Computational Modeling of Crack Initiation in Cross-roll Piercing

by

Sudhir Chiluveru

Submitted to the School of Engineering
in partial fulfillment of the requirements for the degree of

Master of Science in Computation for Design and Optimization

at the

MASSACHUSETTS INSTITUTE OF TECHNOLOGY

June 2007

Author .....
.....
School of Engineering
May 24, 2007

Certified by .....
Raúl A. Radovitzky
Associate Professor, Aeronautics and Astronautics
Thesis Supervisor

Accepted by .....
.....
Jaime Peraire
Professor of Aeronautics and Astronautics
Co-Director, Computation for Design and Optimization Program

Computational Modeling of Crack Initiation in Cross-roll Piercing

by

Sudhir Chiluveru

Submitted to the School of Engineering
on May 24, 2007, in partial fulfillment of the
requirements for the degree of
Master of Science in Computation for Design and Optimization

Abstract

The Mannesmann process is the preferred method in the oil industry for fabrication of hollow pipes. The critical phenomenon in this process is the formation of a small round hole at the center of the cylindrical billet ahead of the piercing plug. In this work the crack initiation that leads to the creation of the small hole has been modeled. The Gurson-Tvergaard-Needleman model of porous plasticity is used to simulate the Mannesmann effect. The appearance of a crack at the center of the cylindrical bar is demonstrated and the stress profiles, plastic equivalent strain profiles and porosity distribution during the deformation process are analyzed. The influence of various parameters in the model on the evolution of porosity in the specimen is studied. Other simple ductile fracture criteria that are proposed in literature are also implemented. An interface model for fracture using the discontinuous Galerkin framework combined with a cohesive fracture law is implemented. This approach and its advantages are illustrated in the application of tensile loading of a simple beam specimen.

Thesis Supervisor: Raúl A. Radovitzky
Associate Professor, Aeronautics and Astronautics

Acknowledgments

I thank my advisor, Prof. Raúl Radovitzky, for his guidance over the past 2 years and making this period an excellent learning experience.

The support of the sponsors Tenaris for this project is gratefully acknowledged. I thank Dr. Eduardo Dvorkin and Ing. Teresa Pérez for their invaluable inputs.

To my colleagues Antoine, Ludovic, Nayden, Ram and Zisu, I am grateful for their friendship and help with my research and my understanding of the subject. I thank my friends here in Cambridge and US for making me feel at home far away from home; and the friends at home for making home what it is.

I dedicate this work to my wonderful family for their love, support, joy and inspiration.

Contents

List of Figures

List of Tables

Chapter 1

Introduction

1.1 Motivation and application

The Mannesmann process is the most established method in the industry for producing seamless steel tubes used in the oil industry for extraction. Because of the absence of welding, seamless pipes are more reliable and hence are preferable. They are produced by cross-roll piercing of solid cylindrical bars at very high temperatures. Local failure at the center of the cylindrical billet forming a small hole prior to piercing, is an important step in the Mannesmann process. It is crucial to be able to predict this failure of material at the center of cylinder in the initial stages because it will significantly influence the forces on the piercing plug, the wear on its surface, the optimal position of the plug to prevent oxidation of the tube, the optimal process conditions and thus the quality of the resulting tube. In other words, this initial transient could play a decisive role in determining the steady-state conditions. Despite the large body of industrial experience, further optimizations of the process

parameters are possible only if one can computationally model the crack initiation and if physics-based descriptions of the process details are given.

1.2 Description of the Mannesmann Process

Molten steel is continuously cast and cut into cylindrical bars called 'billets'. The billets are then heated to approximately 1300°C and passed through a cross-roll set up consisting of two barrel shaped rolls, a piercing plug and shoes to support the billet (Figure 1-1). The cross-rolls compress, rotate and pull the billet simultaneously. The

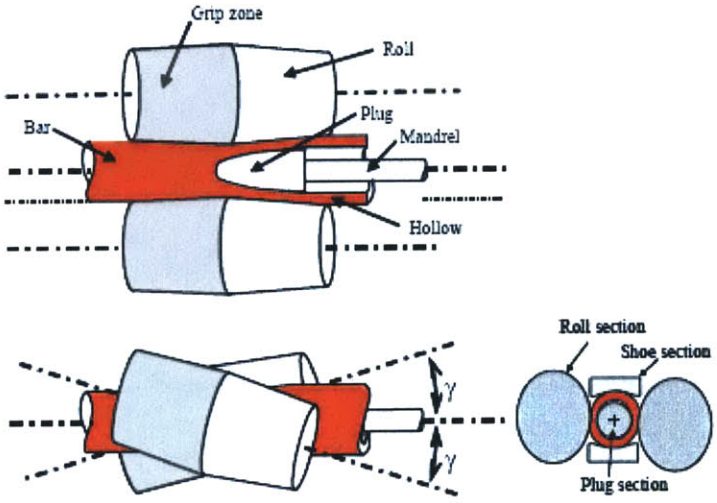

Figure 1-1: Schematic of the Mannesmann setup, taken from [1]

shape of the rolls causes the compression and the angle between the axes of rotation of the rolls (about 4°) causes the pulling. As the compression occurs, the center point of the billet is under tension in horizontal direction, as shown in Figure 1-2. A small cavity appears at the center of the billet because the 'rotating' tensile forces open up a hole at the center [2, 3]. This is called the *Mannesmann effect*. The cavity opens up

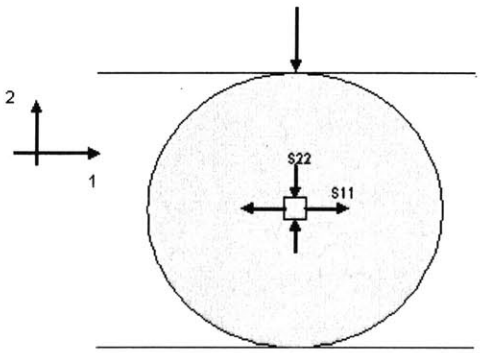

Figure 1-2: Schematic of the stress state at the center of a 2D plate; almost all of the plate is under compressive stress, except along a line parallel to the 2-axis and passing through the center where the stress state is tensile in nature

before the material reaches the nose of the plug. The plug then enables the piercing and flow of material along its surface. Thus steel bars enter the cross-roll setup as billets and leave as shells in less than ten seconds. These shells are subsequently sent through a continuous mill and a stretch reducing mill to prepare them to meet required specifications of thickness, diameter and length.

The position of the fracture initiation affects the service life of the piercing plug. If the fracture in the central part of the billet is not initiated prior to the plug coming into contact with the billet, the forces on the plug and the wear on its surface is excessive and frequent replacements are necessitated. On the other hand, if there is a large gap between the plug and the origin point of the crack, the internal surface of the crack will undergo excessive oxidation leading to defects in the final tube. Hence there is a need to predict the fracture initiation phenomenon to optimize the Mannesmann piercing process in terms of the plug position and other process parameters.

Even in the absence of a piercing plug, the Mannesmann effect is observed [4], thus confirming that the formation of the central hole is not only because of the piercing

action of the plug. In fact, the Mannesmann effect is also observed in a similar metal forming technique called cross wedge rolling, which is used in the fabrication of stepped cylindrical parts from billets [3]. There is no piercing action in this fabrication method and yet undesirable voids appear at the center of the stepped shafts due to the Mannesmann effect.

1.3 Mechanism of void formation in the Mannesmann Process

The Mannesmann process occurs at a temperature of approximately 1300°C. At such high temperatures, steel is highly ductile in nature and deforms due to creep. Analysis of the fracture surface of semi-pierced billet shows both ductile fracture and cleavage zones [4], as shown in Figure 1-3. The high temperature and low tensile stresses of the process would favor ductile fracture perhaps with some associated creep deformation. In this work, it has been assumed that the fracture process is ductile in nature.

1.4 Prior modeling work

Attempts have been made to simulate the cross-roll piercing process using conventional plasticity material models. Urbanski and Kazanecki [5] analyzed the strain distribution in the Mannesmann process using two-dimensional FEM. Capoferri *et al.* [6] and Ceretti *et al.* [7] studied the initiation of voids at the center using 2D simulations and a fracture criterion based on maximum principal stress. Ceretti *et*

al. [8] extended the work to three dimensional modeling.

In Pietsch and Thieven's work [9], hole formation was due only to the piercing plug, making it similar to an extrusion process. Komori [10] simulated the piercing process using a rigid-plastic material model. While the effects of variation of rolling conditions such as the feed angle, the minimum roll gap and the maximum plug diameter were studied, the analysis was restricted to the steady state conditions and initiation of the round hole ahead of the plug was assumed rather than modeled. Pater *et al.* [11] conducted a 3D transient analysis of the piercing process using a thermo-mechanical model. Although they observe that the largest tensile stresses are present in the workpiece axis ahead of the plug that could lead to cracks, there is no prediction or analysis of the crack initiation itself.

Berazategui *et al.* [1] implemented a finite-element approach successfully used in metal forming and have focused on continuum descriptions of the steady-state conditions established in the middle sections of the blank. A damaged cone area, in which the elements are removed intentionally, is introduced to approximate the Mannesmann effect.

1.5 Scope and organization of present work

The main objective of this work has been to describe the onset of piercing and thus complement the analysis of the steady state conditions in [1].Models of ductile crack initiation are employed in order to be able to predict and simulate fracture at the center of the cylindrical billet. 3D transient simulations are carried out in order

to study the crack initiation leading to hole formation ahead of the piercing plug. Using ductile failure models, an attempt is made to provide a physical basis for the description of the Mannesmann effect.

Fracture can be simulated mainly in two ways. One is by deleting elements from the mesh that have exceeded a failure criterion, which is sometimes referred to as the element removal technique. The other is by splitting the mesh nodes at the interface of two elements where failure is calculated to occur. In this work, the first approach is employed by using the Gurson-Tvergaard-Needleman model of porous plasticity and other simple ductile fracture criteria for analyzing the Mannesmann effect. As a contribution to the progress in the modeling of fracture processes, a method has been developed based on the second approach, addressing some of the existing limitations in fracture models based on cohesive theories of fracture and interface elements. It is demonstrated with the example of simple beam specimen under tensile loading.

In Chapter 2, the ductile failure models used in the present work for the analysis of Mannesmann effect are discussed. The models include the Gurson-Tvergaard-Needleman (GTN) model and simple weighted accumulated plastic strain criteria. In Chapter 3, the results of simulation using the GTN model are presented first. Simple 2-dimensional simulations for an initial understanding of stress state and the evolution of porosity are conducted. After providing the geometry, boundary conditions and mesh used for 3D simulations, the stress profiles, equivalent plastic strain contours and void volume fraction (VVF) distribution are analyzed. Similarities in the shapes of the deformed cylindrical billet between the simulations and the actual process are highlighted. The element removal technique is explained. It is demonstrated, using a

set of parameter values, that fracture occurs at the center of the cylinder. A sensitivity analysis of the various parameters involved in the GTN model is done to gain insight into the model. Results of simulations using the simple ductile failure criteria are then presented. The damage limits of these failure criteria are calculated. The influence of stress triaxiality is discussed. Some calibration experiments proposed in the literature that would be useful for these models to be used effectively are mentioned. In Chapter 4 the formulations of cohesive zone modeling (CZM), discontinuous Galerkin (DG) method and a combined method based on these two approaches are presented. The DG based cohesive interface approach is demonstrated in the application of a simple beam specimen under tensile loading. Its advantages are illustrated by considering a problem of uniaxial stress-wave propagation inside the simple beam specimen. In Chapter 5, the work done is summarized and conclusions are drawn. Some directions for further work in this area are provided.

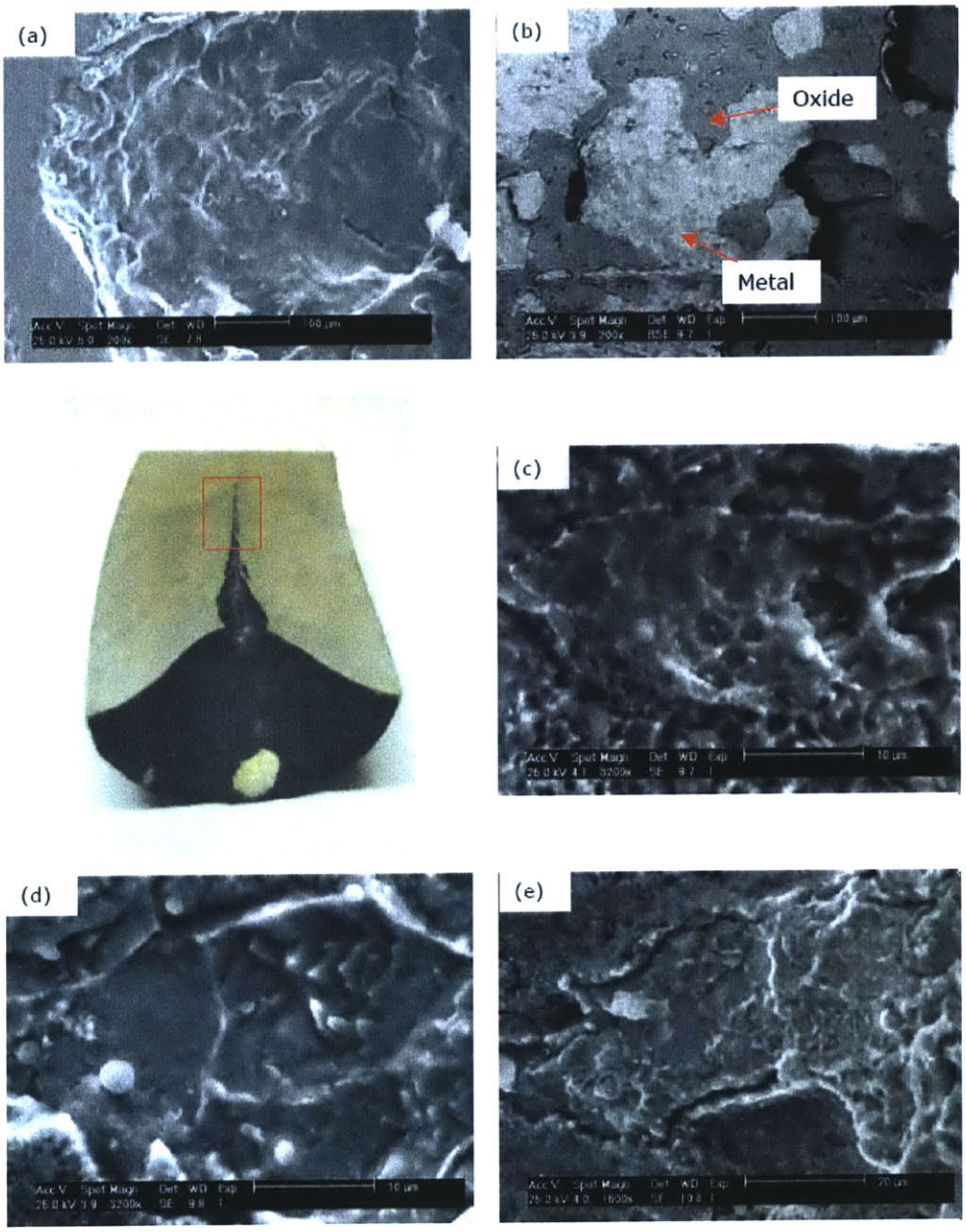

Figure 1-3: Fracture surface of semi-pierced billets (a) 'as polished' (b, c, d, e) after chemical treatment; taken from [4]

Chapter 2

Models of Void Formation in the Mannesmann Process

The Mannesmann process occurs under conditions where the material used is highly ductile in nature. To analyze the initiation of void formation at the center of the cylindrical billet, two types of ductile fracture modeling theories proposed in the literature are employed, namely the Gurson-Tvergaard-Needleman model and weighted accumulated plastic strain criteria. They are both local failure approaches based on damage mechanics, which use accumulated damage as a criterion for crack formation and growth. Material is considered to fail when a damage parameter that depends on local stress and strain fields reaches a critical value [12, 13]. These approaches are in contrast with macroscopic ductile fracture criteria such as J-integral [14, 15], energy release rate R [16], J-Q theory[17, 18], the slip-line solution [19] and crack-tip opening displacement (CTOD) [20] which cannot be readily applied to model crack initiation and growth stages at the microscopic level. While the CTOD criterion depends on

specimen configuration and loading conditions, J-Integral criteria in addition is applicable only to small-scale yielding conditions. The non-material nature of these criteria imposes the drawback that fracture data resulting from simple laboratory tests is not applicable for other specimens and loading conditions that occur in industry.

2.1 Gurson-Tvergaard-Needleman model

Ductile fracture of metals occurs due to growth and coalescence of microscopic voids [12, 21]. Apart from the initial porosity present in the material, new voids are nucleated at inclusions and second phase particles by decohesion or cracking of these particles. The voids grow due to plastic straining of surrounding material under the application of tensile hydrostatic stresses. When material between two neighboring voids is thin enough, it starts to neck resulting in accelerated growth of voids. The voids begin to coalesce, and this results in a crack and subsequent fracture of the material (Figures 2-1,2-2). McClintock[12], Rice and Tracey[13], Gurson[22], Tvergaard and Needleman[23, 24, 25, 26, 27] etc. studied this phenomenon and came up with micromechanical void growth models and macroscopic constitutive models. Gurson's porous metal plasticity model, which was later modified by Tvergaard and Needleman, is the most widely used model amongst these.

The porosity of a material is defined as the ratio of volume of the voids to the total volume of the material. It is denoted by f and is also referred to as the void volume fraction (VVF). It is a measure of damage in the material during the deformation process. The value $f = 0$ corresponds to fully dense material without any voids

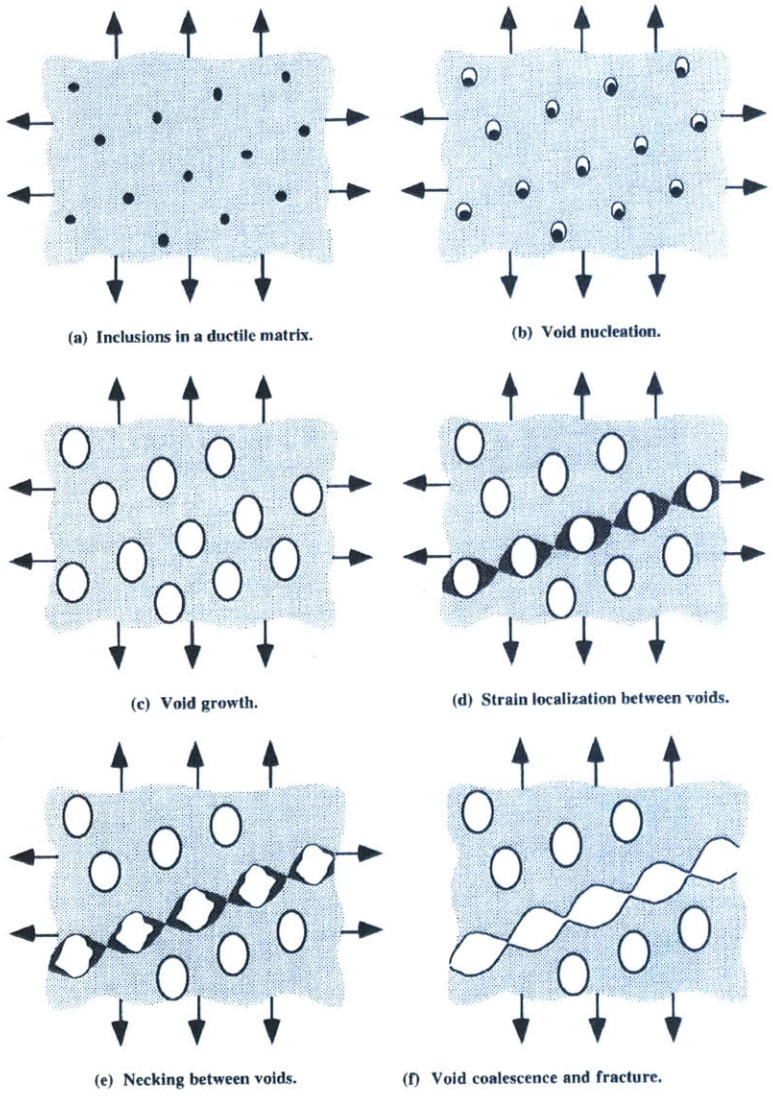

Figure 2-1: Schematic of the nucleation, growth and coalescence of voids, taken from [28]

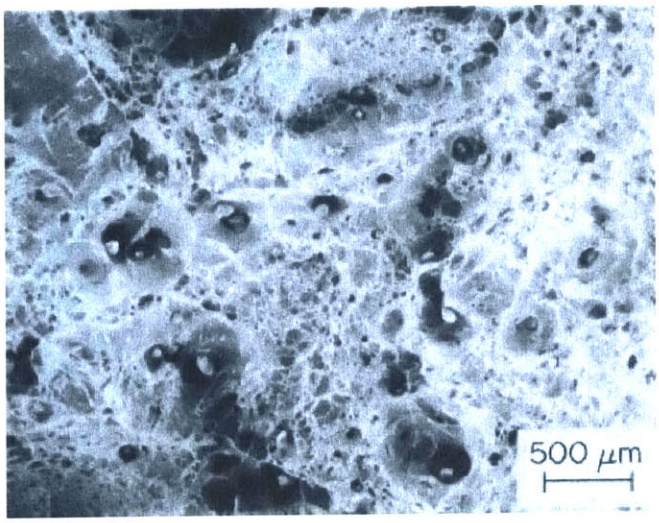

Figure 2-2: Fracture surface at the center of an intially fully dense tensile specimen showing coalesced voids around inclusions and second phase particles, taken from [29]

and the value $f = 1$ corresponds to completely voided material that has no stress carrying capacity. The GTN theory analyzes plastic flow in a porous material by averaging the effect of porosity throughout the material.It is a coupled model, where the accumulated damage influences the material behavior and vice-versa. The damage parameter f therefore appears in the material response relations.

The voids are assumed to be spherical and the material is an aggregate of these spherical voids dispersed in the matrix material randomly. The matrix material is Mises in nature. Mises theory assumes plastic incompressibility and that the hydrostatic component of stress does not effect yield. The dilatation, as observed in processes characterized by large local plastic flow such as those that involve ductile fracture, is entirely due to void growth. In compression the porous material hardens due to closing of the voids, and in tension it softens due to growth of the voids, as shown in Figure 2-3. Here, true stress is plotted on X axis and true strain on the Y

axis and the matrix material is assumed to be elastic-perfectly plastic material. The figure also shows that porous material yields at a lower value of stress. When porosity

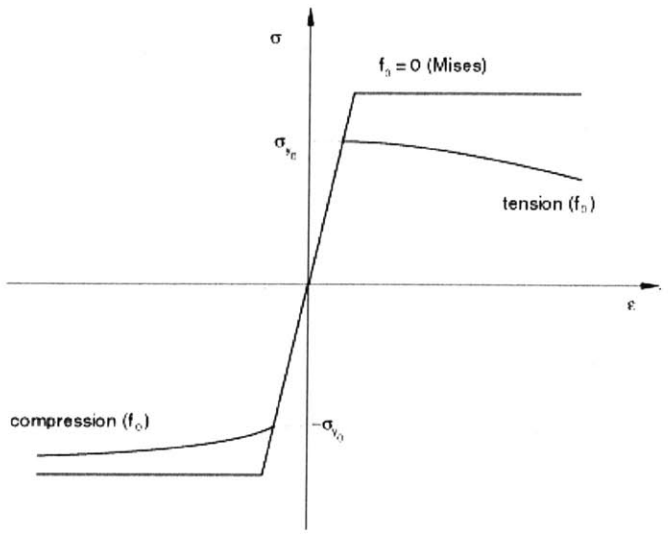

Figure 2-3: Schematic graph comparing uniaxial behavior of porous metals with Mises materials, taken from [30]

is present, hydrostatic stress causes dilatancy and affects plastic yield, as shown in Figure 2-4. In this figure, hydrostatic pressure (scaled by yield stress) is plotted on X axis and equivalent stress (scaled by yield stress)is plotted on Y axis. It is clearly shown that for Mises material ($f = 0$), the yield surface is a straight line implying that hydrostatic stress has no effect. As the porosity increases, the yield surface graph shrinks implying that yielding occurs at lower values of equivalent stress. In fact, it suggests that at very high hydrostatic pressures, yielding occurs even if equivalent stress is zero. The yield condition is of the form

$$\Phi = \left(\frac{\sigma_{eq}}{\sigma_y}\right)^2 + 2q_1 f^* cosh\left(\frac{3}{2}q_2\frac{p}{\sigma_y}\right) - \left(1 + (q_1 f^*)^2\right) = 0 \qquad (2.1)$$

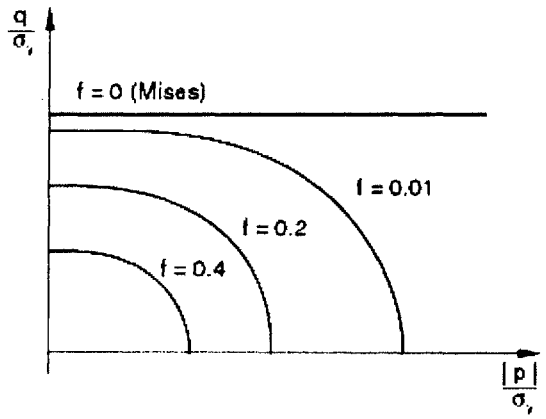

Figure 2-4: Schematic graph comparing yield surface of porous metals with Mises materials, taken from [30]

where σ_{eq} is the equivalent stress defined by $\sigma_{eq} = \sqrt{\frac{3}{2}\mathbf{T}_0 : \mathbf{T}_0}$, $\mathbf{T}_0 = \mathbf{T} + p\mathbf{I}$ is deviatoric part of Cauchy stress tensor $\mathbf{T}$, $p = -\frac{1}{3}\mathbf{T} : \mathbf{I}$ is the hydrostatic pressure, σ_y is the yield stress of the matrix material (which is a function of equivalent plastic strain in the matrix $\bar{\varepsilon}_m^{pl}$). Here f^* is a modified value of porosity f where the modification accounts for the rapid loss of stress carrying capacity due to void coalescence (Figure 2-5) in the following way:

$$f^* = \begin{cases} f & \text{if } f \leq f_c \\ f_c + \frac{\frac{1}{q_1} - f_c}{f_F - f_c}(f - f_c) & \text{if } f_c < f < f_F \\ \frac{1}{q_1} & \text{if } f \geq f_F \end{cases} \tag{2.2}$$

where f_c is the critical value of void volume fraction where void coalescence begins to occur and f_F is the value of void volume fraction at which the material fails.

It is evident that for $f = 0$, equation 2.1 reduces to the classical yield condition $\sigma_{eq} = \sigma_y$.

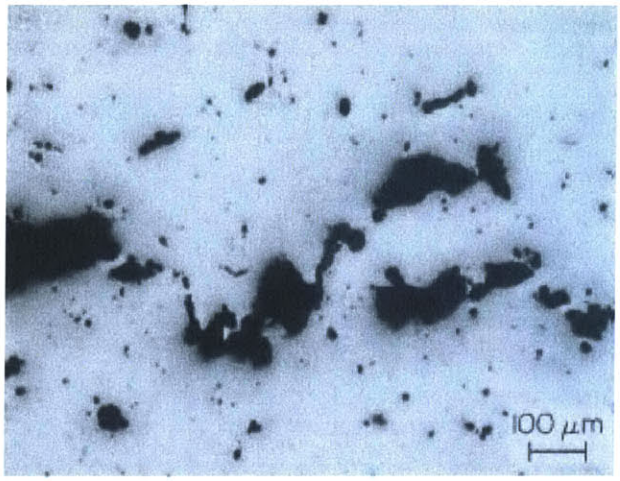

Figure 2-5: Fracture surface of an initially fully dense notched bar showing void coalescence, taken from [29]

The parameters q_1 and q_2 amplify the effect of hydrostatic stress on yielding. They are material specific and can be calibrated to match experimental results by numerical techniques [31]. For typical metals at room temperature, the values of the parameters reported in literature are $1.0 \leq q_1 \leq 2.0$ and $q_2 = 1.0$ [26, 27, 32, 33, 31]. As usual, plastic flow is assumed to be normal to the yield surface:

$$\dot{\varepsilon}^{pl} = \dot{\nu} \frac{\partial \Phi}{\partial \mathbf{T}} \tag{2.3}$$

The hardening of matrix material is described through $\sigma_y = \sigma_y \left(\bar{\varepsilon}_m^{pl}\right)$. For example, a power law can be assumed. The plastic work is expressed as:

$$(1 - f)\, \sigma_y \dot{\bar{\varepsilon}}_m^{pl} = \sigma : \dot{\varepsilon}^{pl} \tag{2.4}$$

The above relation gives the evolution of equivalent plastic strain. Since change in

porosity of the material is due to the combination of growth and nucleation, the evolution of void volume fraction is given by:

$$\dot{f} = \dot{f}_{gr} + \dot{f}_{nucl} \tag{2.5}$$

where $\dot{f}_{gr}$ is change due to growth of existing voids and $\dot{f}_{nucl}$ is change due to nucleation of new voids. The law of conservation of mass requires:

$$\dot{f}_{gr} = (1 - f)\,\dot{\varepsilon}^{pl} : \mathbf{I} \tag{2.6}$$

Nucleation is assumed to be strain controlled and normally distributed [23] in the following way:

$$\dot{f}_{nucl} = \mathbf{A}\dot{\bar{\varepsilon}}^{pl}_{m} \tag{2.7}$$

where

$$\mathbf{A} = \frac{f_N}{s_N\sqrt{2\pi}} e^{-\frac{1}{2}\left(\frac{\bar{\varepsilon}^{pl}_{m} - \varepsilon_N}{s_N}\right)^2} \tag{2.8}$$

Nucleation strain is normally distributed with mean values ε_N and standard deviation s_N as parameters. f_N is the maximum volume fraction of the nucleated voids. Also, voids can nucleate only during tension. As Equation 2.8 suggests, the nucleation function A/f_N is assumed to have a normal distribution. For the same mean ε_N, a higher standard deviation s_N results in a flatter distribution (Figure 2-6). Finite element analysis of a cylinder under rolling and compression is performed using the GTN model to study the Mannesmann process. It is presented in Chapter 3. The results

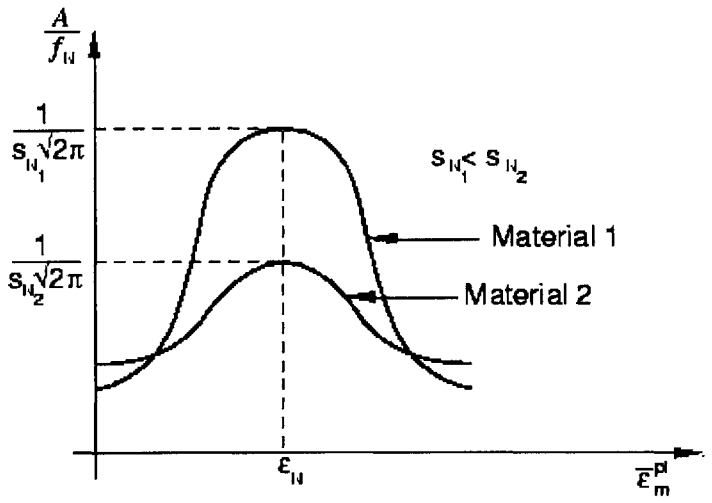

Figure 2-6: Distribution of the nucleation function, taken from [30]

of the simulation showing stress profiles, equivalent plastic strain contours, distribution of VVF and its evolution are examined to understand the physical mechanisms preceding the Mannesmann effect.

2.2 Damage models based on accumulated plastic strain

Many uncoupled ductile crack formation criteria have been proposed in the literature. They estimate that fracture occurs when weighted accumulated plastic strain reaches a critical value:

$$\int_0^{\bar{\varepsilon}_f} f\,(\text{stress state})\, d\bar{\varepsilon} = C \tag{2.9}$$

where f is a weighting function that depends on the stress state in the material locally, $\bar{\varepsilon}$ is the equivalent strain, $\bar{\varepsilon}_f$ is the equivalent strain to fracture and C is a

material constant that needs to be calibrated. Uncoupled models assume that there is no influence of the accumulated damage on the material constitutive response. The damage parameter calculation is thus a procedure that can be implemented in the post-processing phase. Hence the calibration of these criteria is relatively easier. Some successful criteria belonging to this category are shown in Table 2.1. In this table,

Table 2.1: Uncoupled ductile fracture criteria [34]

Criterion	Formula
Equivalent strain	$\bar{\varepsilon}_f$
Cockroft-Latham-Oh	$\int_0^{\bar{\varepsilon}_f} \frac{\sigma_1}{\sigma_{eq}} d\bar{\varepsilon}$
Hydrostatic stress	$\int_0^{\bar{\varepsilon}_f} \frac{\sigma_m}{\sigma_{eq}} d\bar{\varepsilon}$
Clift	$\int_0^{\bar{\varepsilon}_f} \sigma_{eq} d\bar{\varepsilon}$
Brozzo	$\int_0^{\bar{\varepsilon}_f} \frac{2\sigma_1}{3(\sigma_1-\sigma_m)} d\bar{\varepsilon}$
Rice-Tracey (high stress triaxiality)	$\int_0^{\bar{\varepsilon}_f} \exp\left(\frac{3\sigma_m}{2\sigma_{eq}}\right) d\bar{\varepsilon}$
General Rice-Tracey	$\int_0^{\bar{\varepsilon}_f} 0.558\sinh\left(\frac{3\sigma_m}{2\sigma_{eq}}\right) + 0.008\nu\cosh\left(\frac{3\sigma_m}{2\sigma_{eq}}\right) d\bar{\varepsilon}$
LeRoy	$\int_0^{\bar{\varepsilon}_f} (\sigma_1 - \sigma_m)\, d\bar{\varepsilon}$
McClintock	$\int_0^{\bar{\varepsilon}_f} [\frac{\sqrt{3}}{2(1-n)}\sinh\left(\frac{\sqrt{3}}{2(1-n)}\frac{\sigma_1+\sigma_2}{\sigma_{eq}}\right) + \frac{3}{4}\frac{\sigma_1-\sigma_2}{\sigma_{eq}}] d\bar{\varepsilon}$

σ_1 and σ_2 are the maximum and intermediate principal stresses; n is the hardening coefficient; $\nu = -2\frac{\dot{\varepsilon}_2}{\dot{\varepsilon}_1} - \dot{\varepsilon}_3$; $\dot{\varepsilon}_1 \geq \dot{\varepsilon}_2 \geq \dot{\varepsilon}_3$ are the principal strain rates. These fracture criteria are less phenomenological and more empirical in nature. A notable feature of these criteria is that they are simpler and contain fewer parameters as compared to the GTN model. Thus they are suitable for application in an industrial environment.

For calibrating the constant C of Equation 2.9 for a material, both experimental and numerical tests have to be performed. The integral is evaluated either as a post-processing step or as an uncoupled internal variable depending on the stress and strain tensors calculated at a material point. The failure point is determined from

Table 2.2: Equivalent strain to fracture and average stress triaxiality for typical tensile and upsetting tests, taken from [34]

Specimen	Equivalent strain to fracture $\bar{\varepsilon}_f$	Average stress triaxiality $\left(\frac{\sigma_m}{\sigma_{eq}}\right)_{av}$
Upsetting, $d_0/h_0 = 0.5$	0.45	-0.273
Upsetting, $d_0/h_0 = 1$	0.36	-0.236
Tensile, smooth	0.45	0.4
Tensile, $r = 12$ mm	0.28	0.64
Tensile, $r = 4$ mm	0.16	0.95

the experiments. For example, in upsetting tests, cracks form in the equatorial area [35] and can be observed easily. In the case of tensile tests where the crack initiates at the center of the necking region and which cannot be observed on the surface, the loading process is interrupted frequently and the specimens are sliced and inspected for cracks.

Stress triaxiality plays an important role in ductile fracture. It is the ratio of the hydrostatic stress to the mises stress $\left(\frac{\sigma_m}{\sigma_{eq}}\right)$. This ratio changes quite sharply in a specimen undergoing large deformation, as will be seen in Chapter 3 for the cylindrical billet in the Mannesmann process. In order to measure the effect of stress triaxiality on the fracture phenomenon, an average stress triaxiality parameter defined as follows has proved to be useful [34]:

$$\left(\frac{\sigma_m}{\sigma_{eq}}\right)_{av} = \frac{1}{\bar{\varepsilon}_f}\int_0^{\bar{\varepsilon}_f} \frac{\sigma_m}{\sigma_{eq}} d\bar{\varepsilon} \tag{2.10}$$

where $\bar{\varepsilon}_f$ is the equivalent strain at failure. Table 2.2 shows the average stress triaxiality values for some common tests. In this table d_0 and h_0 are the initial

diameter and height of the upsetting specimens, respectively; r is the notch radius of the tensile specimens. It has been observed that the value C in Equation 2.9 is not a universal constant of the material but is dependent on the average stress triaxiality [34], and most likely on the temperature as well. Based on various compressive and tensile tests on notched specimens, it has been found that the equivalent fracture strain varies with average stress triaxiality as shown in Figure 2-7. Also, the fracture

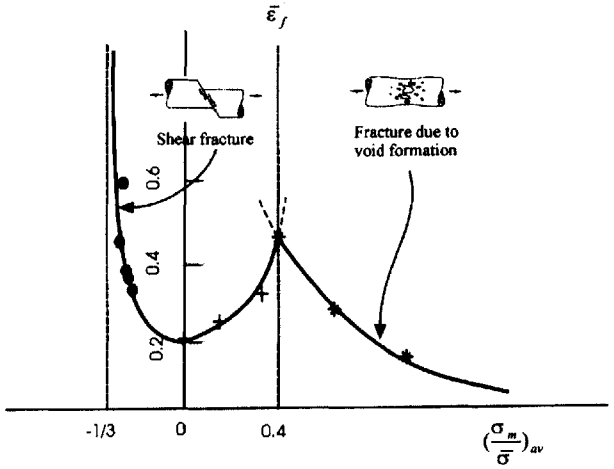

Figure 2-7: Fracture locus in the space of equivalent strain and stress triaxiality, taken from [35]

mechanism itself depends on triaxiality. For processes where triaxiality is high, the mechanism of fracture is ductile in nature due to void growth and coalescence. For negative stress triaxiality (upsetting tests), shear decohesive fracture through the matrix material is observed. The Rice-Tracey, hydrostatic stress and McClintock criteria are based on assumptions of growth of spherical voids, and hence work well for tests in the high stress triaxiality range while Cockroft-Latham-Oh criterion works well for upsetting tests.

Finite element analysis of a cylinder under rolling and compression is performed

in conjunction with these failure criteria. The analysis is presented in Chapter 3. The damage limit constants of these failure criteria are calculated and comparisons with a simple tensile test are provided.

Chapter 3

Finite Element Analysis of the Mannesmann Effect

Finite element analysis using the continuum models proposed in Chapter 2 has been done to simulate the Mannesmann effect. In this chapter the results of these simulations are presented. They are performed using the commercial FEM software ABAQUS/Explicit. The piercing plug is not part of the simulations because only the initial stage of the Mannesmann process is studied.

3.1 Gurson-Tvergaard-Needleman model results

As stated before, the tensile stress state at the center of the the cylindrical billet is a key factor in the Mannesmann process. To verify this claim, a simple two dimensional compressive rolling test has been simulated. The specimen is a circular plate of radius 39.6 mm. Velocity boundary conditions are applied as shown in Figure 3-1(a). The

mesh consists of quadrilateral plane stress elements. A fairly coarse mesh has been used as shown in Figure 3-1(b) because the interest is in qualitative results in these 2D simulations. The material properties used for this simulation are shown in Table 3.1. The stress-strain curve input given for the model is the one corresponding to the lowest strain rate of Figure 3-2. The values of other parameters of the GTN model have been taken from literature [23, 24, 26].

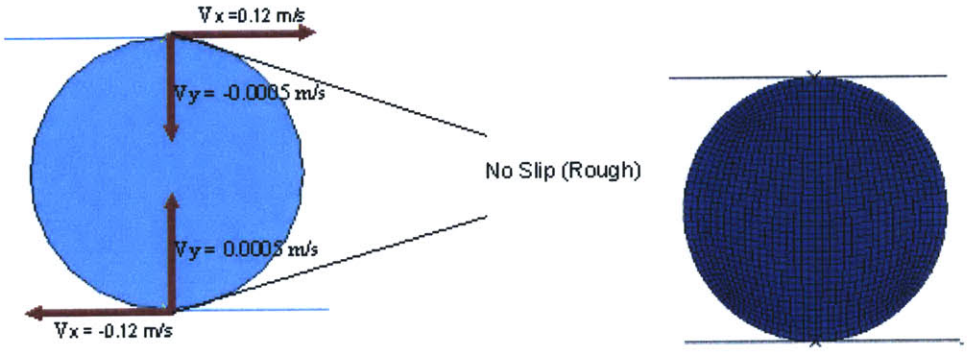

(a) Boundary conditions (b) Mesh

Figure 3-1: 2D simulation setup

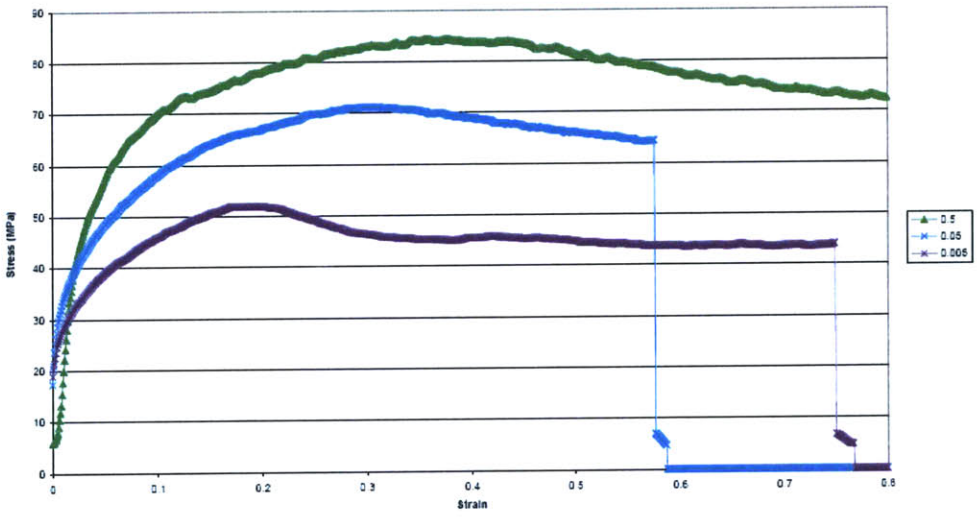

Figure 3-2: Experimental stress-strain curves, taken from [1]

Table 3.1: Material properties used in the GTN model

Property	Value
Density	7800 kg·m^{-3}
Young's modulus	1 GPa
Poisson ratio	0.3
f_0	0.01
f_c	0.15
f_F	0.25
f_N	0.04
ε_N	0.2
s_N	0.075
q_1	1.5
q_2	1.0
q_3	2.25

The results of the 2D simulations are shown below. Figure 3-3 plots the σ_{11} stress contours at various stages of compression in the simulation. Clearly, the σ_{11} tensile stress is maximum at the center of the circular plate at each stage of the compression.

A contour plot of equivalent plastic strain is shown in Figure 3-4. The equivalent plastic strain is maximum at the periphery of the circular plate. This plastic strain is caused due to large compressive stresses, as opposed to the comparatively very small strains at the center of the circular plate caused by a tensile stress state.

Figure 3-5 plots the contours of porosity in the material at various stages of compression showing the evolution of VVF. It is always maximum at the center and close to zero at the periphery. The evolution of VVF due to nucleation (VVFN) and evolution of VVF due to growth (VVFG) show similar trends (Figures 3-6(a), 3-6(b)). Although nucleation is plastic strain controlled, holes nucleate only in tension. Hence nucleation is maximum toward the center of the plate and becomes negligible

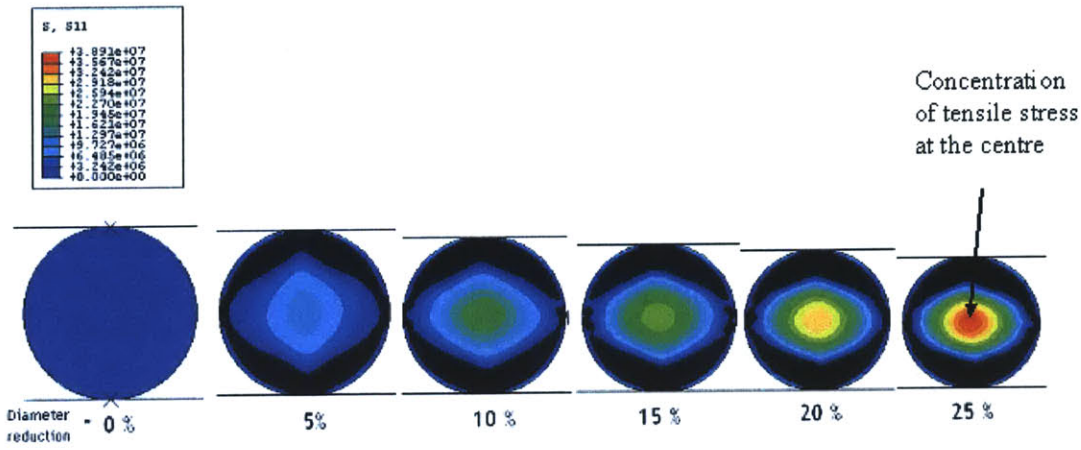

Figure 3-3: 2D simulation results showing contour plot snapshots of σ_{11} stress; the tensile stress is maximum at the center of the plate at each stage of deformation

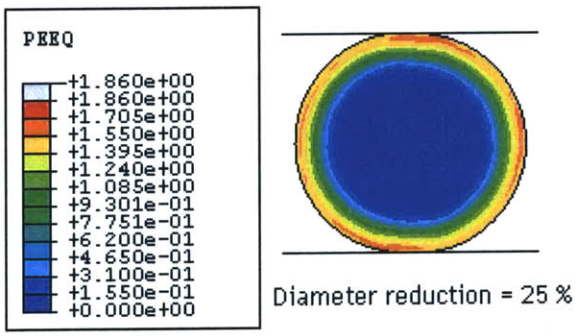

Figure 3-4: Contour plot of equivalent plastic strain; it is maximum at the periphery and minimum at the center

closer to the periphery where the stresses, although high, are compressive in nature. The growth of voids depends on hydrostatic stresses. Tensile hydrostatic stresses enlarge the voids while compressive hydrostatic stresses shrink them. Hence, VVFG is also maximum at the center and negligible at the periphery. The combined effect of VVFN and VVFG is that VVF is maximum at the center and decreases toward the periphery.

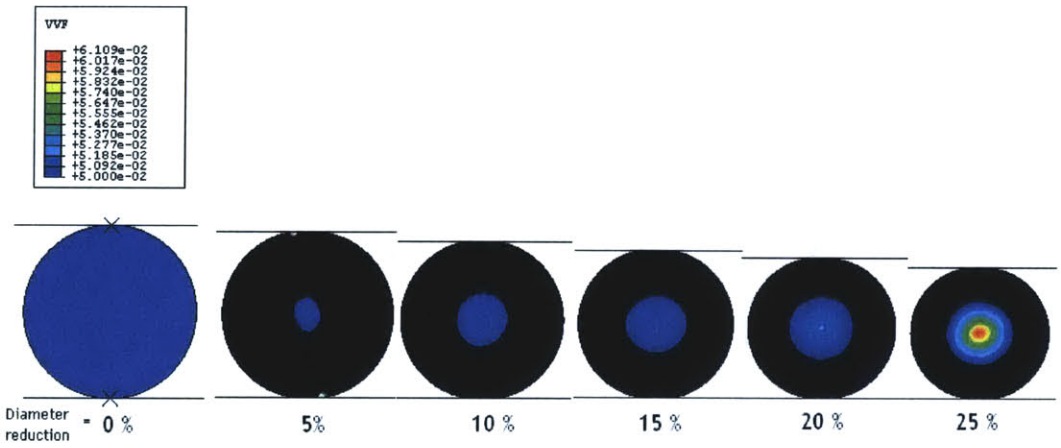

Figure 3-5: Evolution of total VVF for the 2D simulation

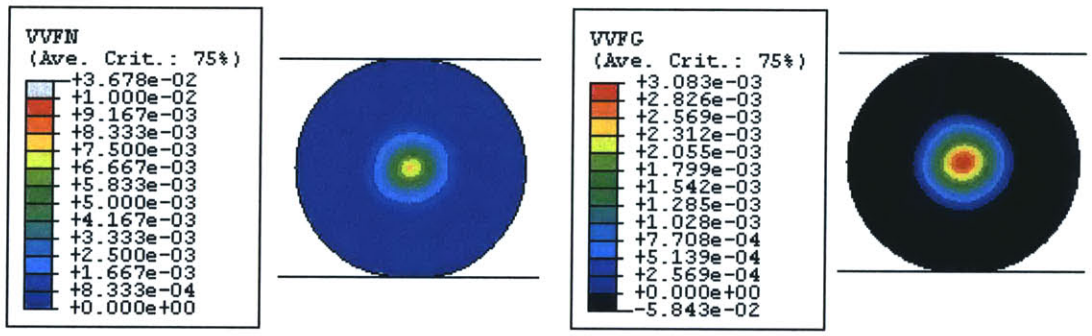

(a) VVF due to nucleation

(b) VVF due to growth

Figure 3-6: Contour plots of VVF components for the 2D simulation at 25% diameter reduction

Some aspects of the Mannesmann process are not captured in 2D simulations.

Figure 3-7 shows how a semi-pierced billet has a radially symmetric trough at the ends. To capture such effects, and also to get closer to more realistic process conditions, three dimensional simulations are carried out.

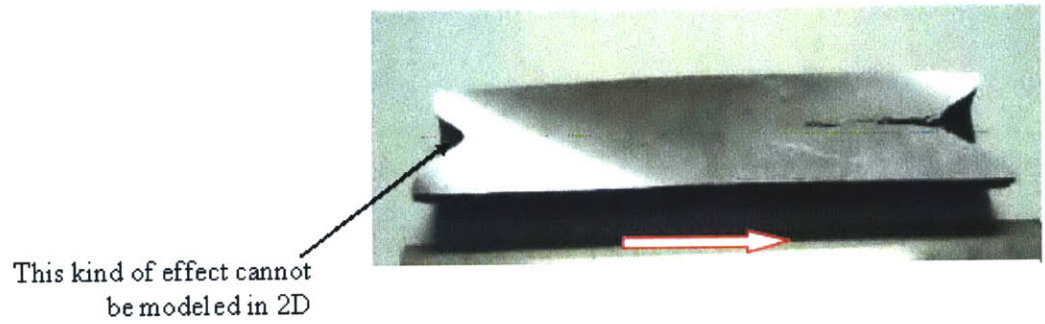

Figure 3-7: Cross-section of a cylindrical billet after cross-rolling showing a curved surfaces at either ends, taken from [4]

The three dimensional cross-roll setup can be created in a standard FEM package by modeling the rolls as rigid analytical surfaces in the shape of drums and oriented at an angle with each other, as shown in Figure 3-8. The cylindrical billet is in contact with both rolls. In this geometric model, the shoes preventing lateral expansion and movement of the billet are ignored. Instead, the axis of the cylinder is constrained to move only in the y-direction so as to reduce wobbling. There is contact friction between the surfaces of the cylinder and the drums. When the drums are rotated about their axes, the cylinder gets pulled in and compressed simultaneously, emulating the actual Mannesmann process.Figure 3-9 shows the deformed mesh at the final time step of a successful Mannesmann process simulation. This figure also shows the torsion of the billet and the end effect at the leading section. The deformed face at the leading edge is also seen to have the maximum VVF at the center.

This geometric model works well, but takes considerable amount of time for sim-

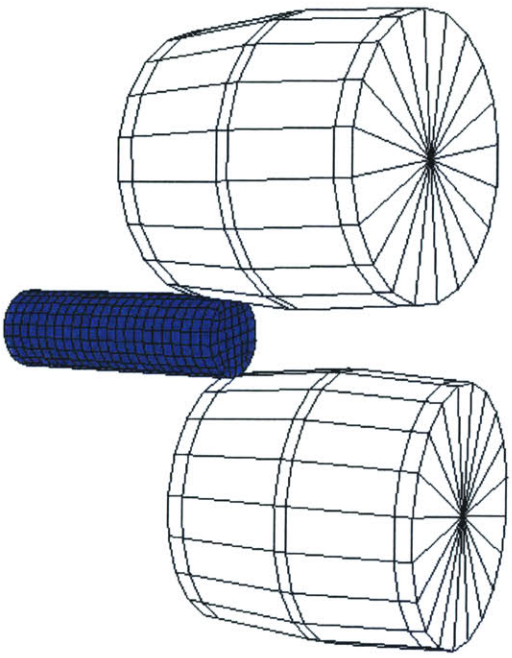

Figure 3-8: 3D simulation setup including cross-rollers for the Mannesmann process

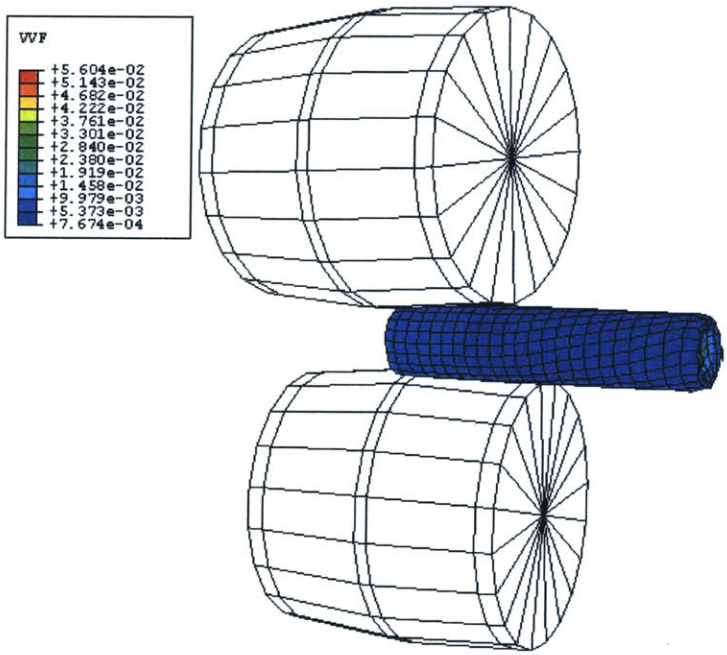

Figure 3-9: Simulation of the Mannesmann process; the cylindrical billet is pulled in due to the angle between the cross-rolls and is compressed due to their shape

ulations owing to its complexity. In order to model the key features of the onset of piercing without the complexities of the full three-dimensional model, a simplified approach has been devised. The cross-rolling process is approximated through a wedge rolling process as shown in Figure 3-10. Similar to the 2D geometric model discussed earlier, the cylindrical billet is compressed and rolled simultaneously. The stress state inside the material closely replicates the cross-roll conditions. 8-node brick elements are used to mesh the specimen.

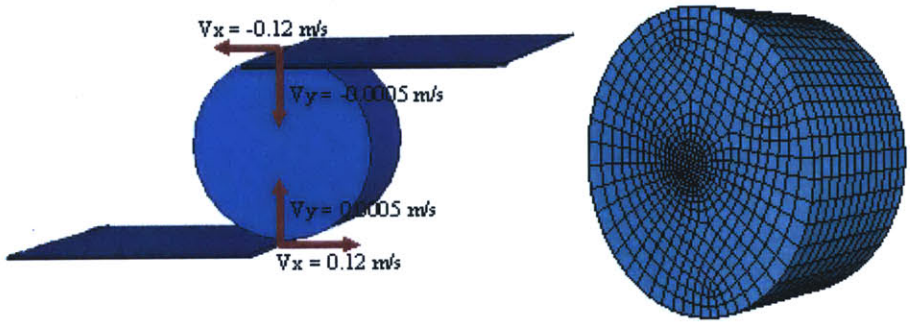

Figure 3-10: Simplified setup and specimen mesh for 3D simulation

Figure 3-11 is a contour plot of a cross-section of the cylinder showing the evolution of σ_{11} stresses as the diameter of the cylinder is reduced up to 25%. The stress state at the center is tensile in nature, and it is the maximum at this location. Toward the periphery of the cylinder, the stresses are compressive in nature.

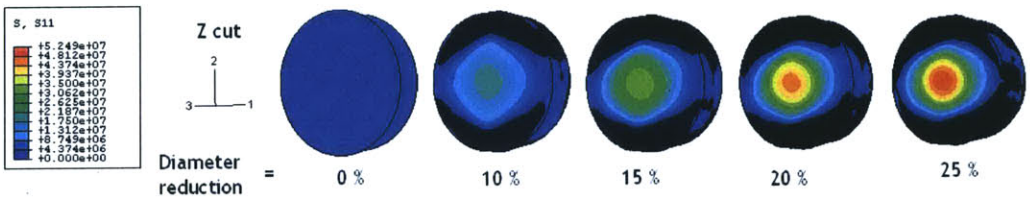

Figure 3-11: Evolution of σ_{11} stresses in the 3D simulation

Figure 3-12 shows the contour plots of the equivalent plastic strain at cross-sections along the Z-plane. It can be noticed that plastic strain is very high along the boundary of the cylinder. Since porosity of the material is negligible here due to compressive hydrostatic stresses, the material cannot undergo volume change and has nowhere to go except to flow longitudinally along the axis of the cylinder. This is consistent with the observations in practice of troughs on the faces of the billet in cross-rolling (Figure 3-7). The specimen in the simulations also deforms in a similar fashion as shown in Figure 3-13.

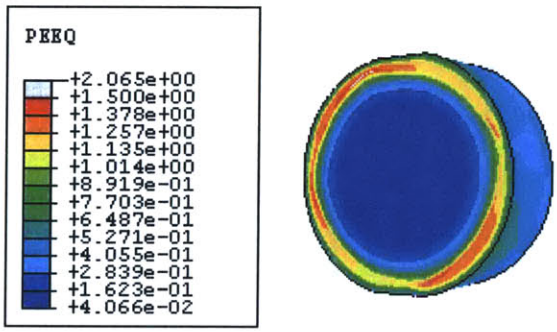

Figure 3-12: Contour plot of equivalent plastic strain at a cross-section in the 3D simulation

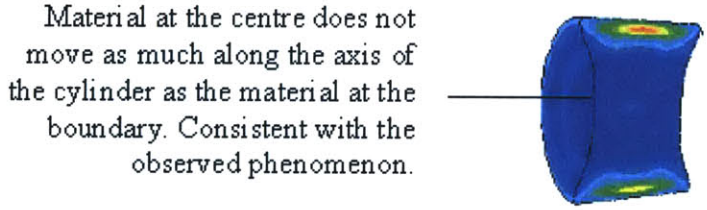

Figure 3-13: Deformed shape of the cylinder in the 3D simulation

In order to model the onset of void formation, a popular approach for modeling fracture within the finite element codes known as the element removal technique [26, 36] is employed. Under this approach, a damage parameter for each element is

calculated and tracked and the element is considered to fail when a fracture criterion is reached. In the GTN model, the fracture criterion is based on the VVF approaching a failure limit. Once an element fails, it is unable to sustain any load and can undergo any amount of deformation without affecting the neighboring elements. In other words, the element is completely removed from the simulations. This approach of fracture simulation is available in ABAQUS/Explicit [30] and is adopted in this work. As expected, the fracture phenomenon has mesh dependency. The finer the mesh, the more accurate the fracture process is in the simulations.

The simulations show that VVFG is maximum at the center and decreases away from it (Figure 3-14). In the GTN model, nucleation is 'tensile strain' controlled. Figure 3-15 shows that VVFN is maximum midway between the center and periphery, an aspect that was not captured by the 2D model. This is because the σ_{33} tensile stresses and the resulting strains are highest in this region of the specimen. Nevertheless, the value of VVFN near the center is also high in comparison. The combined effect

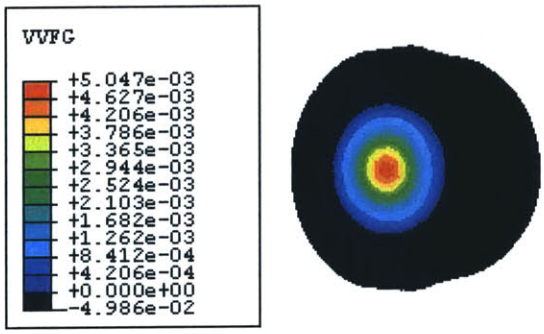

Figure 3-14: Contour plot of VVFG in the 3D simulation

is that total VVF is maximum at the center of the cylinder. Figure 3-16 shows the evolution of VVF at a cross-section at various stages of deformation of the cylinder.

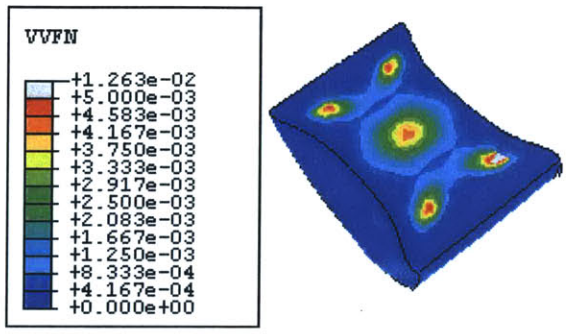

Figure 3-15: Contour plot of VVFN in the 3D simulation

In these simulations $f_N = 0.20$, $\varepsilon_N = 0.05$ and the values of other parameters are from Table 3.1. For this set of parameters, the last snapshot in Figure 3-16 shows that when the diameter reduction is 18% the elements at the center of the cylinder have reached the fracture criterion $f = 0.25$, resulting in fracture along the axis of the cylinder.

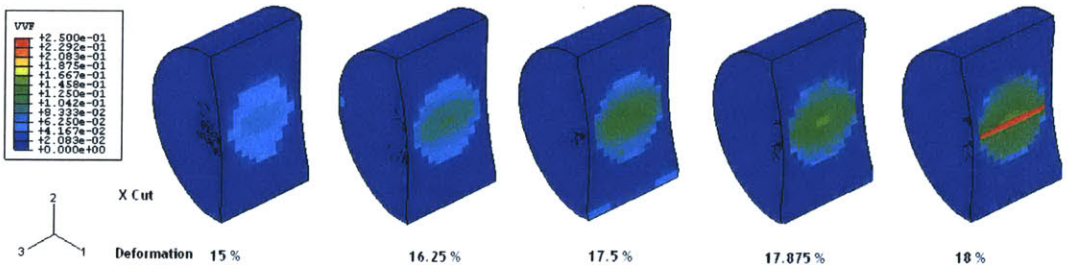

Figure 3-16: Evolution of VVF in the 3D simulation; fracture at the center is demonstrated

In addition to the parameters involved in the classical plasticity model, the GTN model includes 8 parameters: porosity parameters (f_0, f_c, f_F), nucleation parameters $(f_N, \varepsilon_N, s_N)$ and curve-fitting material parameters (q_1, q_2). It is important to study the effects of these parameters on the model to gain a deeper understanding of the GTN theory.

Figure 3-17 shows the evolution of total VVF (of an element at the center that fails first) plotted against diameter reduction for three different sets of parameters. For high f_N and low q_2, nucleation dominates throughout the deformation process. For low f_N and low q_2, nucleation dominates initially until it flattens out after reaching a max value of f_N. Growth of existing voids then dominates the contribution to total VVF. For low f_N and high q_2, growth portion dominates throughout. Thus the evolution of porosity in the model depends heavily on values chosen for the parameters.

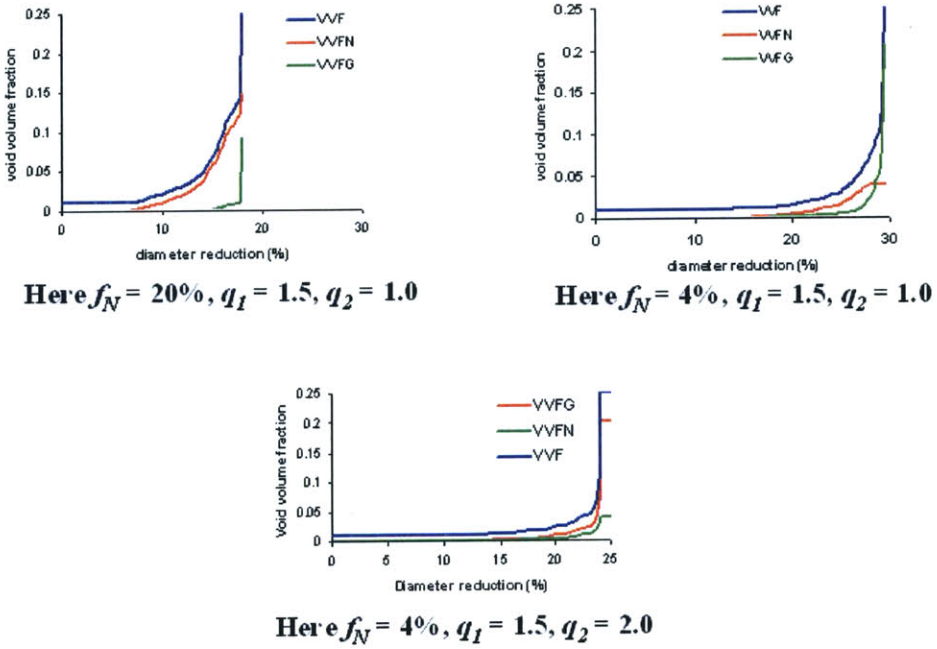

Figure 3-17: Effect of parameters f_N and q_2 on the evolution of VVF at the center of the cylindrical specimen

As expected, diameter reduction for failure decreases with increase in f_0 and f_N, and increases with f_c, as shown in Figure 3-17. Except for very small values of ε_N, the diameter reduction required for failure increases with increasing ε_N. The reason is

evident from the distribution of the nucleation function as shown in Figure 2-6. The area under this curve up to a particular equivalent strain $\bar{\varepsilon}_m^{pl}$ represents the VVFN. For large values of ε_N, the peak is far from the origin and large deformations are necessary to achieve large VVFN. For very small values of ε_N, the bell shape of the nucleation function is truncated at the $\bar{\varepsilon}_m^{pl} = 0$ axis because voids nucleate only in tension. Hence the diameter reduction for failure increases slightly for very small values of ε_N.

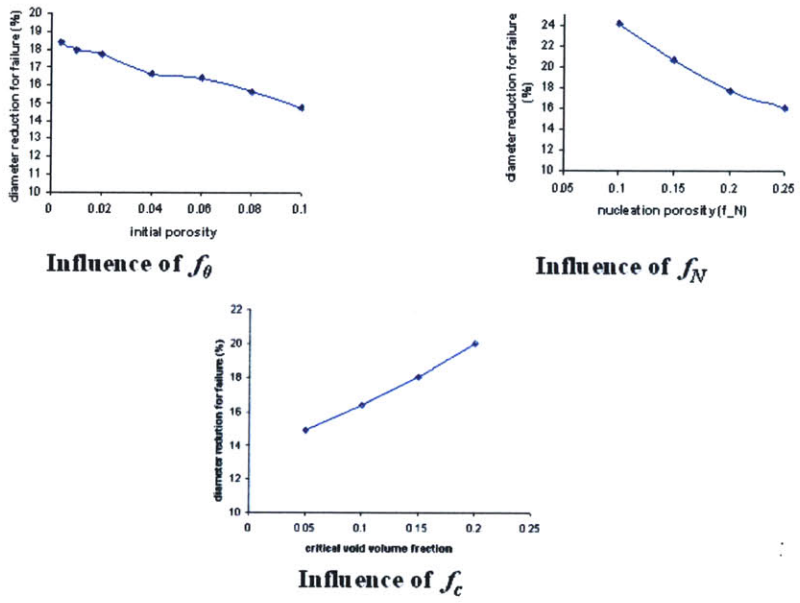

Figure 3-18: Effect of parameters f_0, f_c and f_N on diameter reduction for failure

Some practical considerations in implementing the GTN model are mentioned here. The input data for GTN model consists of Young's modulus, Poisson ratio, yield stress, stress-strain curve, porosity parameters (f_0, f_c, f_F), nucleation parameters $(f_N, \varepsilon_N, s_N)$ and curve fitting parameters (q_1, q_2). While there are established experimental tests for obtaining the parameters of the conventional plasticity model,

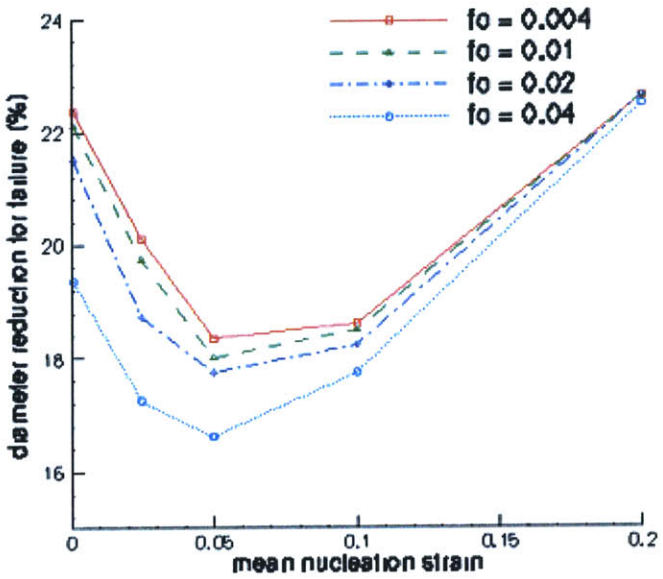

Figure 3-19: Effect of parameter ε_N on diameter reduction for failure

it is less clear how to obtain the parameters of the porous GTN model. Calibration of f_0, f_N and f_F can in principle be done using metallurgical tests involving optical microscopy and image processing techniques [37]. However, it is difficult to precisely measure these values. Values of 0.15 and 0.25 have been reported for f_F [37]. Also, because of the idealizations in the model, f_0 determined from metallurgical studies may not be directly relevant. The critical porosity f_c is dependent on the values chosen for other parameters. A fitting procedure can be applied to determine f_c after the other parameters have been selected first. The value of f_c for which the load drop point is the same for both numerical simulations and experimental results is identified. Another method for determining f_c is by using an analytical cell model with constant stress triaxiality [38, 39, 40]. The equations can be integrated in a semi-analytical way to determine when there is necking in the unit cell model, thereby identifying f_c.

These selected parameters are usually verified by different notched tensile specimens and then used in other applications. However, some of these parameters could be influenced by stress triaxiality [41, 42, 43] and temperature. In particular, a constant critical porosity may not be an accurate criterion at low to mid triaxialities [44]. The values of the parameters for materials at high temperatures of the order of 1300°C are not available in literature and have to be found out experimentally. Indeed, it has been found that the selection of some of the parameters is not unique in parameter fitting when using finite element models [38].

The GTN model does not predict failure under shear. Low stress triaxiality conditions are unfavorable for the GTN model because the assumptions in this model are usually valid in high triaxiality conditions such as those in simple tensile tests. Also, modifications in the model are needed to account for void shapes, void spacing and void orientations [45, 44].

3.2 Modeling results of simple ductile fracture criteria

Uncoupled ductile criteria are simpler owing to the fact they can be implemented as a post-processing step of traditional finite element method. The analysis of stress-triaxiality at the center of the cylinder in the simple 3D rolling test is carried out first. Classical plasticity model is used for the material behavior. Figure 3-20 shows the evolution of triaxiality at the center. It can be seen that as the deformation increases,

the triaxiality increases too. Also, the triaxiality is negative in the beginning.

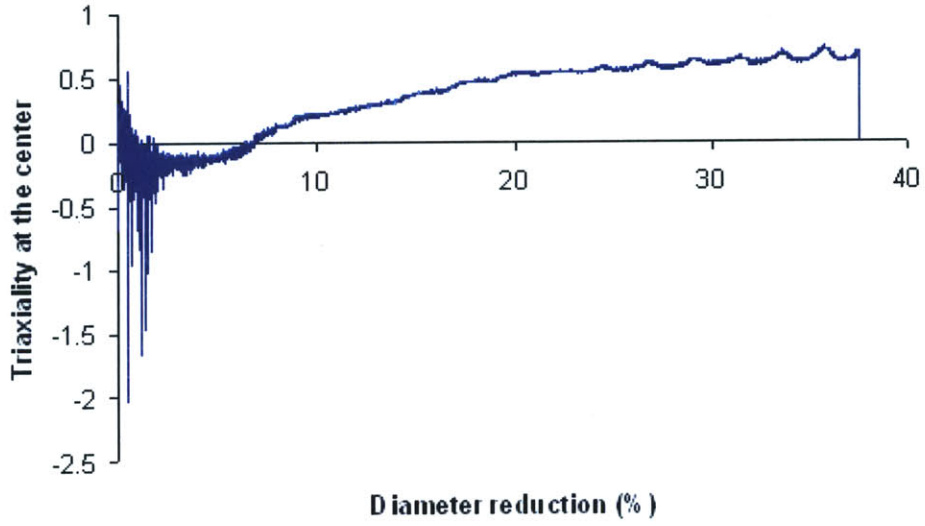

Figure 3-20: Stress triaxiality at the center of the cylinder plotted against diameter reduction

To compare the wedge rolling test with a simple tensile test, an axisymmetric tensile test is simulated. The geometry and mesh of the tensile specimen is shown in Figure 3-21. The same material as that of the 3D rolling test is used. The specimen is pulled up to the point of necking and fracture, when there is an abrupt drop in the load - displacement curve.

Experimental studies [4] have suggested that fracture in non-plug cross-rolling occurs at about 15% diameter reduction of the cylinder. Hence in the 3D rolling test, it is assumed that fracture occurs at 15% diameter reduction to enable comparison with the tensile test and to calculate the calibration constants of the various fracture criteria of Table 2.1. As shown in Table 3.2, the two processes are considerably

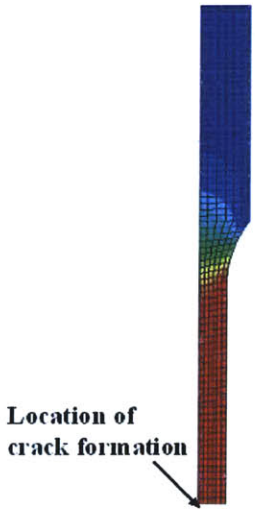

Figure 3-21: The geometry and mesh of the 2D tensile specimen

Table 3.2: Comparing the tensile test and simple 3D rolling test

	Tensile test	3D Rolling test (Fracture assumed to occur at 15% diameter reduction)
Average stress triaxiality of failed element	0.41	0.24
Equivalent strain to fracture	0.313	0.042

different in terms of average stress triaxiality. Also, the equivalent strain to fracture is almost an order of magnitude lower in the 3D rolling simulation case.

Assuming fracture at the center of the cylinder at 15% diameter reduction in the simple 3D rolling test, the values of the calibration constants C of Equation 2.9 have been calculated according to the formulae of Table 2.1. The results are presented in Table 3.3. The constants are calculated for the simple tension test too for comparison. It can be seen that the calibration constants are much lower for the 3D rolling test which is expected because of lower average triaxiality conditions. In order to verify the values for the calibration constants obtained for the 3D rolling

Table 3.3: Calibration constants for the uncoupled ductile failure criteria, evaluated for tensile test and simple 3D rolling test

Fracture Criterion	Tensile test	3D Rolling test
Equivalent strain	0.313	0.042
Cockroft-Latham-Oh	0.337	0.038
Hydrostatic stress	0.128	0.010
Clift	1.414E+07	0.126E+07
Brozzo	4.049E+03	0.398E+03
Rice-Trace for high triaxiality	0.209	0.033
General Rice-Tracey	0.050	0.009
LeRoy	2.108E+07	0.148E+07
McClintock (hardening coeff = 0.05)	0.601	0.064

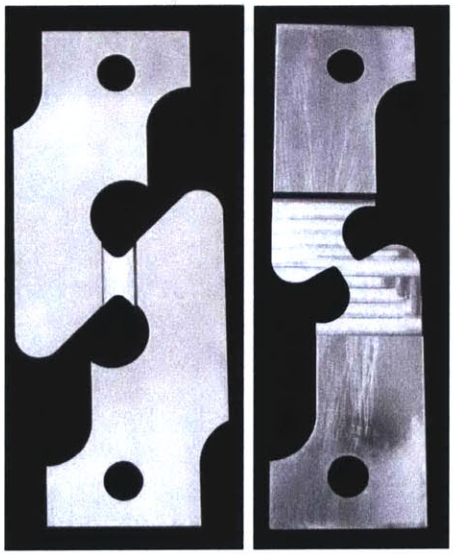

(a) Low triaxiality (b) Medium triaxiality

Figure 3-22: Specimens suggested by Bao and Wierzbicki [35] for low to medium stress triaxiality condition tests

test, the fracture criteria need to be calibrated using experiments and numerical simulations of processes that have similar average stress triaxialities. To be able to predict crack initiation in the Mannesmann process, one approach is to use the non-plug piercing experiments and simulations for one particular case of the Mannesmann process, calculate the fracture criteria constants and use these calibrated constants for predicting fracture for other geometries and conditions. Another approach is to perform simpler tests that have similar average stress triaxiality. For very low stress triaxialities, Bao and Wierzbicki [35] suggest that a pure shear test can be performed, as shown in Figure 3-22(a). For low to moderate stress triaxialities they suggest a combined shear and tensile loading test, as shown in Figure 3-22(b).

Chapter 4

Interface Model based on the Discontinuous Galerkin Method

The Mannesmann effect was modeled using the element removal method in the previous chapter. A more fundamental approach to modeling the initiation of fracture under the conditions of the Mannesmann process consisting of modeling the micromechanisms of intra and intergrain fracture at high temperature may be pursued. This requires the ability to describe fracture within the finite element framework with more detail than available in the element removal technique. The best established approach in this direction is based on cohesive theories of brittle fracture, in which cracks are modeled explicitly at the interelement boundaries via specialized interface elements endowed with a fracture mechanics based traction-separation law [46].

In this approach of modeling fracture, crack initiation and propagation is allowed along predefined cohesive surfaces that are embedded in the material along likely crack propagation paths along the internal surfaces of a discretized body [46, 47].The

cohesive layer opens up when the stresses in the adjoining bulk elements exceed a cohesive limit, and from then on the thickness of the cohesive element represents the extent of the crack during the deformation process.

There are some problems associated with this approach. A constitutive law of the interface chosen is in general independent of the constitutive behavior in the bulk of the solid. Hence the cohesive interface formulation introduces unphysical numerical quantities in the stiffness matrix and can lead to problems in wave propagation [48]. The effect of this inconsistency can be minimized by choosing a high initial stiffness of the cohesive law. But this requires small time steps to avoid instabilities in dynamic simulations and relaxation of the assumption that the cohesive law is a material property [48]. In this work, it is proposed to address this problem by formulating the interface elements within the discontinuous Galerkin (DG) framework.

In the DG method, the problem unknowns are allowed to have discontinuities at the interelement boundaries in a consistent manner. It is superior to the continuous formulation in modeling fracture because one can represent the discontinuities that appear in the solution. The versatility of the DG method is evident in the fact that recent efforts in this field include applications to non-linear elasticity [49], beams and plates [50], shells [51], fracture [52] and non-local theories of damage [53]. Computations involving wave propagation, high strain rates and large plastic deformations have been carried out to demonstrate and verify the robustness of the method [54]. Apart from being convenient to be implemented along with conventional finite element methods, the DG method also lends itself to easy parallel implementation [54] and is highly scalable.

Mergheim *et al.* [52] proposed an approach to model fracture that combines the discontinuous Galerkin method in the pre-failure regime with the CZM approach in the post-failure regime. This formulation eliminates the problems with the cohesive approach discussed earlier while inheriting the advantages of the DG method. In this chapter, this *hybrid* approach is applied to an example of simple elastic beam specimen under tensile loading. Simulation of the Mannesmann process using this method is left for future work.

The formulations of the DG method, cohesive theory and the proposed combined approach are now presented. To begin with, the boundary value problem of static finite deformations of elastic bodies is written as follows [55]:

$$\nabla_0 \cdot \boldsymbol{P} + \rho_0 \mathbf{B} = \mathbf{0} \text{ in } B_0 \tag{4.1}$$

$$\boldsymbol{\varphi} = \bar{\boldsymbol{\varphi}} \text{ on } \partial_D B_0 \tag{4.2}$$

$$\boldsymbol{P} \cdot \mathbf{N} = \bar{\mathbf{T}} \text{ on } \partial_N B_0 \tag{4.3}$$

where $B_0 \subset \mathbb{R}^3$ is the region of space occupied by the body in its reference configuration, $\boldsymbol{P}$ is the first Piola-Kirchhoff stress tensor, $\rho_0 \mathbf{B}$ are the body forces per unit reference volume, ∇_0 is the material gradient operator, $\boldsymbol{\varphi}$ is the deformation mapping, $\mathbf{N}$ is the unit surface normal in the reference configuration and $\bar{\boldsymbol{\varphi}}$ and $\bar{\mathbf{T}}$ are the boundary conditions applied on the displacement $\partial_D B_0$ and traction $\partial_N B_0$ parts of the boundary, respectively.

For numerical discretization, the body B_0 is approximated by a discretized domain (mesh) B_{0h} as shown in Figure 4-1.

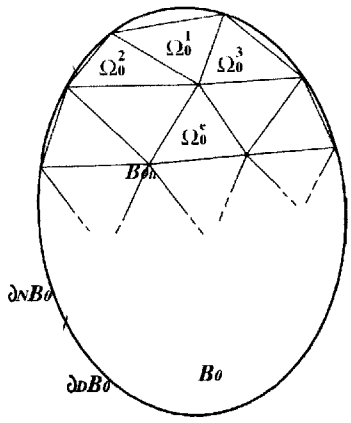

Figure 4-1: Schematic of the discrete representation of elastic domain B_0 as a subdivision B_{0h}, taken from [49]

4.1 Formulation of the DG method

In the DG method, the problem unknowns are allowed to have discontinuities at interelement boundaries. Henceforth the subscript h added to any symbol denotes the finite element approximation of the corresponding entity and exists in an appropriate space that differs from the conventional finite element space in that it allows for jump discontinuities at interelement boundaries.

The strong form (Equation 4.1) is multiplied with a test function $\delta\boldsymbol{\varphi}_h$ and integrated by parts over the the domain B_{0h} to obtain:

$$\begin{aligned} &\int_{B_{0h}} \boldsymbol{P}_h : \boldsymbol{\nabla}_0 \delta\boldsymbol{\varphi}_h dV + \int_{\partial_I B_{0h}} [\![\delta\boldsymbol{\varphi}_h]\!] \cdot \langle \boldsymbol{P}_h \rangle \cdot \boldsymbol{N} dS = \\ &\int_{B_{0h}} \rho_0 \boldsymbol{B} \cdot \delta\boldsymbol{\varphi}_h dV + \int_{\partial_N B_{0h}} \delta\boldsymbol{\varphi}_h \cdot \bar{\boldsymbol{T}} dS \quad \forall \delta\boldsymbol{\varphi}_h \in \mathrm{X}^k_{\mathrm{hc}} \end{aligned} \tag{4.4}$$

where $[\![\bullet]\!]$ and $\langle\bullet\rangle$ denote the jump and mean respectively in a generic field $\bullet$ at the boundary of two elements. This weak form is neither symmetric nor stable.

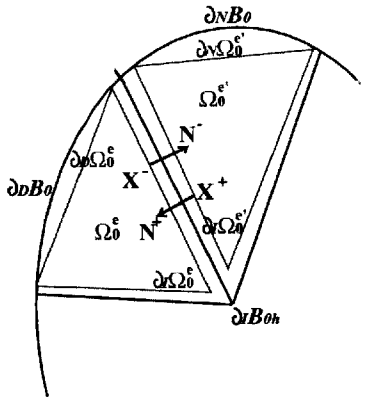

Figure 4-2: Details of two elements Ω_0^e and $\Omega_0^{e'}$ of the discretization B_{0h}, taken from Noels and Radovitzky [49]; $\partial_D B_0$ is the Dirichlet boundary, $\partial_N B_0$ is the Neumann boundary, $\partial_I B_{0h}$ is the interior boundary of the discretization; the outward normals of the two elements are represented

A symmetrization term and a penalty term (to stabilize the method) are added to Equation 4.4 resulting in the following final weak form of the DG formulation:

$$\begin{aligned}
&\int_{B_{0h}} \boldsymbol{P}_h : \boldsymbol{\nabla}_0 \delta\boldsymbol{\varphi}_h dV + \int_{\partial_I B_{0h}} \left([\![\boldsymbol{\varphi}_h]\!] \cdot \langle \mathbb{C} : \boldsymbol{\nabla}_0 \delta\boldsymbol{\varphi}_h \rangle \cdot \boldsymbol{N} + [\![\delta\boldsymbol{\varphi}_h]\!] \cdot \langle \boldsymbol{P}_h \rangle \cdot \boldsymbol{N} \right) dS \\
&\qquad + \int_{\partial_I B_{0h}} [\![\delta\boldsymbol{\varphi}_h]\!] \otimes \boldsymbol{N} : \left\langle \frac{\beta}{h_s} \mathbb{C} \right\rangle : [\![\boldsymbol{\varphi}_h]\!] \otimes \boldsymbol{N} dS = \\
&\int_{B_{0h}} \rho_0 \boldsymbol{B} \cdot \delta\boldsymbol{\varphi}_h dV + \int_{\partial_N B_{0h}} \delta\boldsymbol{\varphi}_h \cdot \bar{\boldsymbol{T}} dS \quad \forall \delta\boldsymbol{\varphi}_h \in \mathrm{X}_{\mathrm{hc}}^k
\end{aligned} \tag{4.5}$$

The DG formulation can easily be extended to dynamic problems [54]. Even in the presence of physical discontinuities in the material, the DG method provides a rigorous means of ensuring both consistency and stability. Consistency is guaranteed because of the use of average numerical fluxes at the interface and stability is ensured by appropriate quadratic terms in the weak formulation. Also, using the DG approach one can rigorously enforce the continuity requirement weakly in theories requiring higher-order continuity such as gradient theories of plasticity. The

consistency, linearized stability in the non-linear range and the convergence rate of the method have been proved [49]. Computations involving wave propagation, high strain rates and large plastic deformations have been carried out to demonstrate and verify the robustness of the method [54].

4.2 Formulation of the cohesive interface approach

In the cohesive zone modeling (CZM) method, fracture is regarded as a phenomenon in which separation takes place in a cohesive zone at a crack tip when the separating forces exceed cohesive traction limits [56, 57, 14]. A cohesive fracture law can thus be formulated giving a relation between an effective opening displacement δ and traction t as shown in Figure 4-3. The weak form of Equation 4.4 is the basis of the formulation

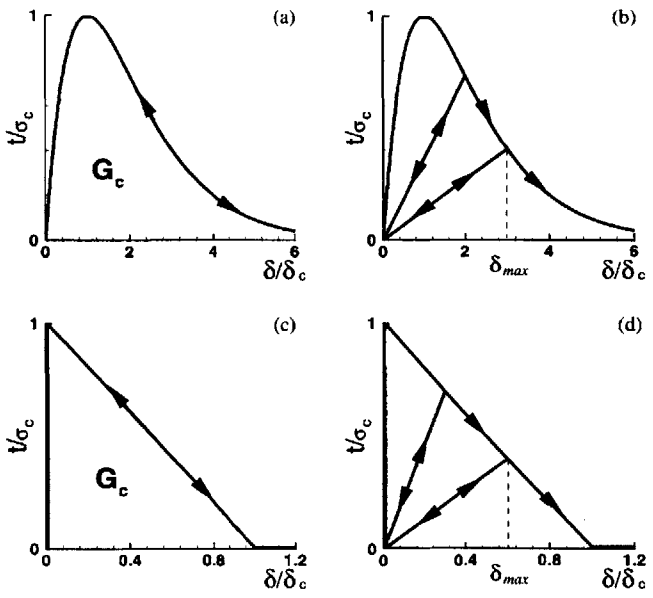

Figure 4-3: Examples of cohesive laws relating normalized effective opening displacement δ and effective traction t, taken from [46] (a)Reversible Smith-Ferrante (b)Irreversible Smith-Ferrante (c)Reversible linear (d)Irreversible linear

for the cohesive interface approach. The material behavior across an inter-element boundary is governed by a traction-separation law of the interface and the cohesive formulation is written as:

$$\int_{B_{0h}} \boldsymbol{P}_h : \boldsymbol{\nabla}_0 \delta\boldsymbol{\varphi}_h dV + \int_{\partial_I B_{0h}} [\![\delta\boldsymbol{\varphi}_h]\!] \cdot \boldsymbol{t}\left([\![\boldsymbol{\varphi}_h]\!]\right) dS =$$

$$\int_{B_{0h}} \rho_0 \boldsymbol{B} \cdot \delta\boldsymbol{\varphi}_h dV + \int_{\partial_N B_{0h}} \delta\boldsymbol{\varphi}_h \cdot \bar{\boldsymbol{T}} dS \quad \forall \delta\boldsymbol{\varphi}_h \in \mathrm{X}^k_{\mathrm{hc}} \tag{4.6}$$

where the traction vector $\boldsymbol{t}$ is determined as a function of the opening displacement $[\![\boldsymbol{\varphi}_h]\!]$ according to a chosen cohesive law. Specifically, the traction vector is divided into normal and tangential components as:

$$\boldsymbol{t} = t_n \boldsymbol{N} + t_m \boldsymbol{M} \tag{4.7}$$

where $\boldsymbol{M}$ is a tangential vector of the mid-interface. An exponential cohesive law of Smith-Ferrante type can be written as:

$$t_n(\delta) = \frac{\sigma_c}{\delta_c} \mathrm{e}^{(1-\delta/\delta_c)} \delta_n \tag{4.8}$$

$$t_m(\delta) = \gamma^2 \frac{\sigma_c}{\delta_c} \mathrm{e}^{(1-\delta/\delta_c)} \delta_s \tag{4.9}$$

where $\delta_n = [\![\boldsymbol{\varphi}_h \cdot \boldsymbol{N}]\!]$ and $\delta_s = [\![\boldsymbol{\varphi}_h \cdot \boldsymbol{M}]\!]$ are the normal and tangential components respectively of the interelement jump, $\delta = \sqrt{\gamma^2 {\delta_s}^2 + {\delta_n}^2}$ is an effective opening displacement as seen in Figure 4-3, γ is a parameter assigning different weights to the normal and tangential opening displacements, σ_c is the maximum cohesive normal

traction and δ_c is a characteristic opening displacement.

The maximum cohesive traction is nothing but the spall strength of the material and the area under the cohesive law is its fracture energy. Thus the theory incorporates a physical basis. It is noteworthy that no assumption needs to be made of any particular type of constitutive response in the bulk of the material, the extent of crack growth or the size of plastic zone. Also, there are no assumptions of the direction of crack propagation and its shape except that cracks can only propagate along element boundaries. Under dynamic loading conditions, this theory automatically accounts for rate-dependency of fracture [58].

A constitutive law of the interface thus chosen is independent of the constitutive behavior in the bulk of the solid. This inconsistency can lead to problems in wave propagation [48]. The formulation of the cohesive approach within the DG framework that addresses this problem is now presented.

4.3 The discontinuous Galerkin based interface approach for modeling fracture

The idea of this approach is that the DG method ensures the weak enforcement of the continuity of the solution along the interface prior to failure and the cohesive interface approach controls the jump in the displacements after the failure occurs. This is done by combining the DG approach with the cohesive interface approach [52] with a switching factor based on a fracture criterion being met. A binary factor α is

used to obtain the weak formulation of the proposed method as:

$$\int_{B_{0h}} \boldsymbol{P}_h : \boldsymbol{\nabla}_0 \delta\boldsymbol{\varphi}_h dV + \alpha\{\int_{\partial_I B_{0h}} [\![\delta\boldsymbol{\varphi}_h]\!] \cdot t\left([\![\boldsymbol{\varphi}_h]\!]\right) dS\}$$

$$+ (1-\alpha)\{\int_{\partial_I B_{0h}} \left([\![\delta\boldsymbol{\varphi}_h]\!] \cdot \langle \mathbb{C} : \boldsymbol{\nabla}_0 \delta\boldsymbol{\varphi}_h \rangle \cdot \boldsymbol{N} + [\![\boldsymbol{\varphi}_h]\!] \cdot \langle \boldsymbol{P}_h \rangle \cdot \boldsymbol{N}\right) dS +$$

$$\int_{\partial_I B_{0h}} [\![\delta\boldsymbol{\varphi}_h]\!] \otimes \boldsymbol{N} : \left\langle \frac{\beta}{h_s} \mathbb{C} \right\rangle : [\![\boldsymbol{\varphi}_h]\!] \otimes \boldsymbol{N} dS\} =$$

$$\int_{B_{0h}} \rho_0 \boldsymbol{B} \cdot \delta\boldsymbol{\varphi}_h dV + \int_{\partial_N B_{0h}} \delta\boldsymbol{\varphi}_h \cdot \bar{\boldsymbol{T}} dS \quad \forall \delta\boldsymbol{\varphi}_h \in \mathrm{X}^k_{\mathrm{hc}} \tag{4.10}$$

The parameter values $\alpha = 0$ in the pre-failure regime and $\alpha = 1$ in the post-failure regime are chosen. The failure criterion is:

$$\boldsymbol{P}_h : [\boldsymbol{N} \otimes \boldsymbol{N}] + \gamma \boldsymbol{P}_h : [\boldsymbol{N} \otimes \boldsymbol{M}] - \sigma_c > 0 \tag{4.11}$$

For a smooth transition from DG method to interface approach, the values $\boldsymbol{P}_h : [\boldsymbol{N} \otimes \boldsymbol{N}]$ and $\boldsymbol{P}_h : [\boldsymbol{N} \otimes \boldsymbol{M}]$ are respectively ensured to be the normal and tangential components respectively of $\boldsymbol{t}$ for $[\![\boldsymbol{\varphi}_h]\!] = 0$.

4.4 Finite element implementation

For finite element implementation, the symmetrizing term of the weak formulations is ignored for ease and simplicity of implementation. This term is not necessary as the weak enforcement of the C^0 continuity at element interfaces is already taken care of by the quadratic stabilization term. The weak form then reduces to:

$$\mathbf{f}^{int}(\mathbf{x}) + \mathbf{f}^{I}(\mathbf{x}) = \mathbf{f}^{ext} \tag{4.12}$$

where

$$\mathbf{f}^{int} \cdot \delta\mathbf{x} = \int_{B_{0h}} \boldsymbol{P}_h : \boldsymbol{\nabla}_0 \delta\boldsymbol{\varphi}_h dV \tag{4.13}$$

$$\mathbf{f}^{ext} \cdot \delta\mathbf{x} = \int_{B_{0h}} \rho_0 \boldsymbol{B} \cdot \delta\boldsymbol{\varphi}_h dV + \int_{\partial_N B_{0h}} \delta\boldsymbol{\varphi}_h \cdot \bar{\boldsymbol{T}} dS \tag{4.14}$$

constitute respectively the conventional internal and external virtual work leading to the customary unmodified finite element arrays $\mathbf{f}^{int}$ and $\mathbf{f}^{ext}$ and the interelement boundary terms leading to the following nodal array that contributes to the internal force array:

$$\begin{aligned} \mathbf{f}^{I} \cdot \delta\mathbf{x} = \alpha\{ & \textstyle\int_{\partial_I B_{0h}} [\![\delta\boldsymbol{\varphi}_h]\!] \cdot t\left([\![\boldsymbol{\varphi}_h]\!]\right) dS\} \\ & + (1-\alpha)\{\textstyle\int_{\partial_I B_{0h}} [\![\boldsymbol{\varphi}_h]\!] \cdot \langle \boldsymbol{P}_h \rangle \cdot \boldsymbol{N} dS + \\ & \textstyle\int_{\partial_I B_{0h}} [\![\delta\boldsymbol{\varphi}_h]\!] \otimes \boldsymbol{N} : \left\langle \frac{\beta}{h_s}\mathbb{C} \right\rangle : [\![\boldsymbol{\varphi}_h]\!] \otimes \boldsymbol{N} dS\} \end{aligned} \tag{4.15}$$

Taking the conventional finite element spatial discretization of bodies as a base, zero thickness surface-like interface elements are inserted between the bulk finite elements [59, 60, 46, 49]. In the post-failure regime, thickness of these cohesive elements varies according to a cohesive law, thereby accommodating the cohesive zone approach. The interface element consists of two 6-node surface elements (labeled X^- and X^+) as shown in Figure 4-4(b). These two surfaces coincide in reference space and make up one cohesive element with 12 nodes.

The interpolation of the position, the deformation mapping and its jumps in the reference configuration are performed using the standard shape functions of the sur-

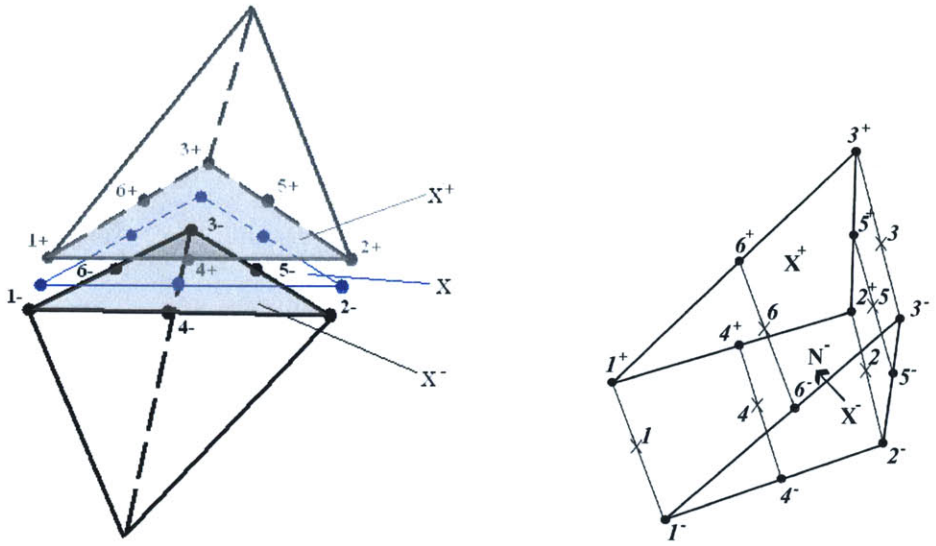

(a) Assembly of a 12-node cohesive element with two 10-node tetrahedral elements

(b) Interface element

Figure 4-4: 12-node interface element compatible with 3D tetrahedral elements

face element $N_a(\boldsymbol{\xi}), a \in [1, n]$, where $\boldsymbol{\xi} = (\xi_1, \xi_2)$ are the natural coordinates. Thus,

$$\mathbf{X}^{\pm}(\boldsymbol{\xi}) = \sum_{a=1}^{n} N_a(\boldsymbol{\xi}) \mathbf{X}_a^{\pm} \tag{4.16}$$

$$[\![\varphi_h]\!](\boldsymbol{\xi}) = \sum_{a=1}^{n} N_a(\boldsymbol{\xi}) \left[\mathbf{x}_a^{+} - \mathbf{x}_a^{-}\right] \tag{4.17}$$

$$[\![\delta\varphi_h]\!](\boldsymbol{\xi}) = \sum_{a=1}^{n} N_a(\boldsymbol{\xi}) \left[\delta\mathbf{x}_a^{+} - \delta\mathbf{x}_a^{-}\right] \tag{4.18}$$

where $\mathbf{X}_a^{\pm}$ and $\mathbf{x}_a^{\pm}, a \in [1, n]$ are the nodal coordinates of the surface elements in the reference and deformed configuration, respectively. The interelement outer surface normal $\mathbf{N}^{-}$ corresponding to element Ω_0^{e-} evaluated on the mid surface is obtained as:

$$\mathbf{N}^{-}(\boldsymbol{\xi}) = \frac{\mathbf{G}_1(\boldsymbol{\xi}) \times \mathbf{G}_2(\boldsymbol{\xi})}{|\mathbf{G}_1(\boldsymbol{\xi}) \times \mathbf{G}_2(\boldsymbol{\xi})|} \tag{4.19}$$

in which

$$\mathbf{G}_\alpha(\boldsymbol{\xi}) = \mathbf{X}_{,\alpha} = \sum_{a=1}^{n} N_{a,\alpha}(\boldsymbol{\xi})\mathbf{X}_a \tag{4.20}$$

are the tangent basis vectors, $\alpha \in [1,2]$, $\mathbf{X}_a = \frac{\mathbf{X}_a^+ + \mathbf{X}_a^-}{2}$ and similarly $\mathbf{x}_a = \frac{\mathbf{x}_a^+ + \mathbf{x}_a^-}{2}$. Further details of the finite element implementation are provided in Noels and Radovitzky [49].

4.5 Application to a beam under tensile loading

In order to demonstrate the proposed interface method, the problem of tensile loading of a beam is considered. Figure 4-5 shows a simple beam with a square cross-section, discretized symmetrically using 10-node quadratic tetrahedral elements. A single layer of interface elements is inserted between the bulk elements at the mid-section of the beam parallel to face 'a' and face 'b'. Faces 'c' and 'd' are constrained along

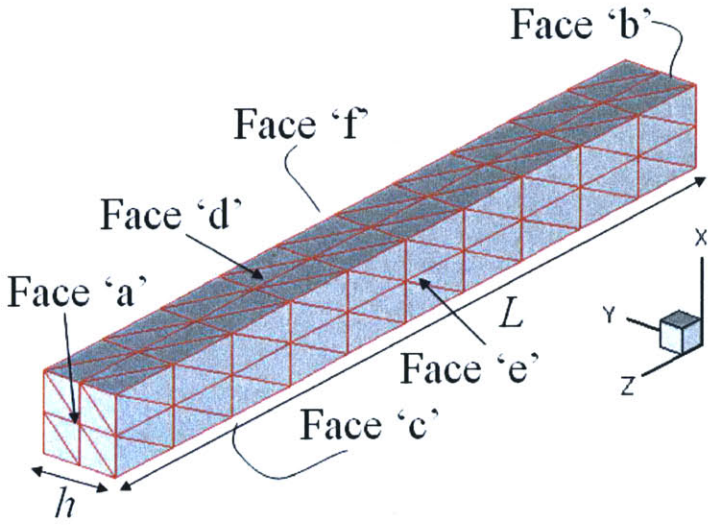

Figure 4-5: Geometry and mesh of a simple beam specimen

Table 4.1: Geometrical and material properties used in the simulation of the propagation of a stress wave in an elastic medium

Properties	Values
Length	$L = 1$ m
Height	$h = 0.1$ m
Density	$\rho_0 = 10000$ kg·m^{-3}
Young modulus	$E = 10000$ N·mm^{-2}
Poisson ratio	$\nu = 0$
Initial velocity	$v_0 = 25$ m·s^{-1}

Table 4.2: Properties of the interface element

Properties	Values
β	4
γ	0.707
σ_c	1000 MPa
δ_c	5.46 μm

X axis, faces 'e' and 'f' along Y axis and face 'b' along Z axis. Face 'a' is imposed with a constant velocity v_0 in the +Z direction. The geometric dimensions, material properties and initial velocity are given in Table 4.1. The values of parameters of the proposed interface law are given in Table 4.2. The cohesive law used in the method is a Smith-Ferrante envelope as shown in Figure 4-3.

The neo-Hookean material model extended to the compressible range is considered without Poisson effect (Table 4.1), so as to make the wave propagation uniaxial in nature. The strain energy density function is

$$W = \left(\frac{\lambda}{2}\log J - \mu\right)\log J + \frac{\mu}{2}(I_1 - 3)\,, \tag{4.21}$$

where λ and μ are the Lamé constants, $J = \det(\boldsymbol{F})$ and $I_1 = tr(\boldsymbol{C})$.

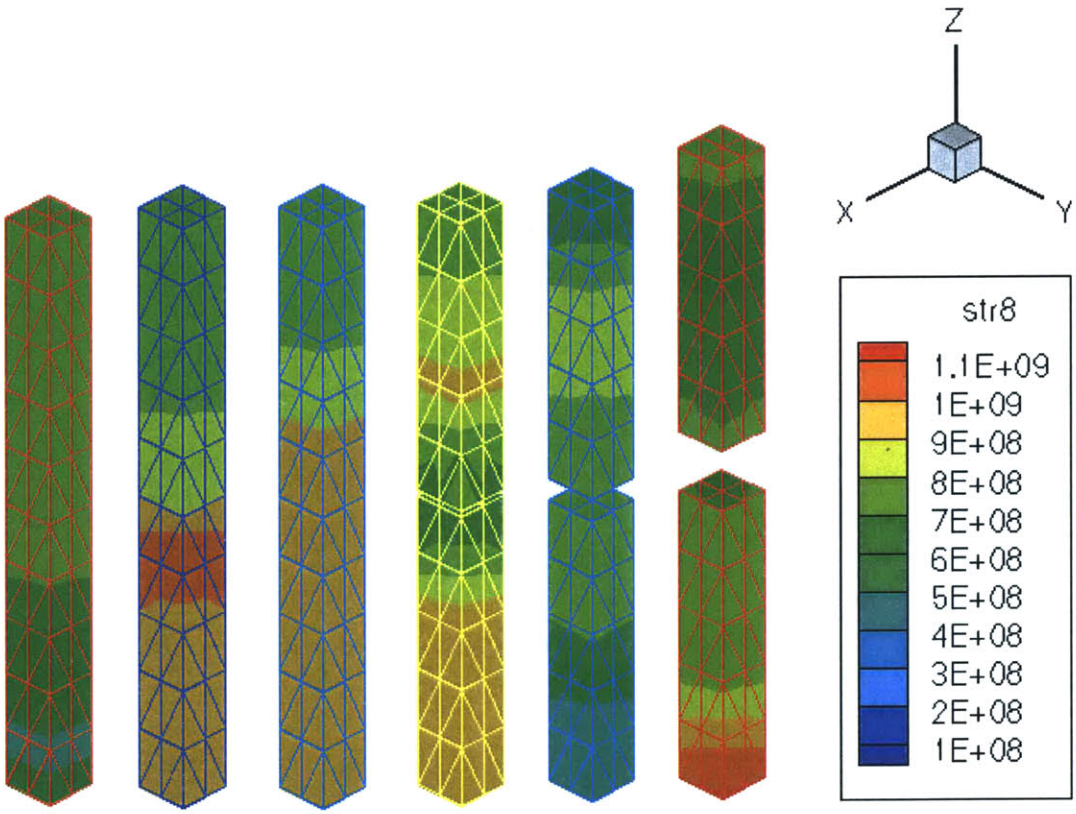

Figure 4-6: Simulation of the beam under tension; contours correspond to σ_{33} stresses; there is a layer of interface elements at the middle of the beam where a crack opens up

Figure 4-6 shows the snapshots of the beam at various stages in the simulation. As the beam gets extended, the deformation gives rise to increasingly large tensile stresses in the beam. At a certain stage these stresses exceed the cohesive limit at the middle of the beam. A crack opens up at the interface layer and the interface elements follow the cohesive law. Because the boundary conditions persist in the simulation, the crack size increases and becomes comparable to the dimensions of the beam itself.

4.6 Stress wave propagation problem

In order to demonstrate the advantages of the DG method based cohesive interface approach over the simple cohesive interface method, the problem of propagation of a uniaxial stress wave in an elastic medium passing through multiple layers of interface elements is considered. The simple beam specimen of Figure 4-5 is used again. There are interface elements between all the bulk elements in this case. The boundary conditions in this case are different too. Instead of face 'a', now the entire specimen is given an initial velocity v_0 in the +Z direction. Again faces 'c' and 'd' are constrained along X axis, faces 'e' and 'f' along Y axis and face 'b' along Z axis. Since face 'b' is constrained along Z axis, a tensile-wave originates there and moves toward face 'a' at the speed of sound. The velocity v_0 in this case is 0.1 m·s^{-1}. In order to exaggerate the difference between the cohesive interface approach and the proposed approach for purpose of clarity, the parameters of the cohesive law in this section are taken as $\sigma_c = 6000$ MPa and $\delta_c = 5.46x10^{-4}$m, where δ_c is far from the optimized value.

At time $t = 0$ a tensile wave originates in face 'b' and propagates towards face 'a' at the speed of sound. It passes through the bulk and interface elements of the beam (Figure 4-7) and reaches face 'a', and the entire beam is under tension. At this stage the velocity of nodes on face 'a' ideally changes from +0.1 m/s to −0.1 m/s and the tensile wave reflects instantaneously. The wave passes through the beam again before reaching face 'b' to complete one cycle of wave propagation. The velocity given to the beam is low, hence the stresses are low such that the interface layer does not open up *i.e.*, there is no fracture. Since there is no fracture, the conventional finite

element (Galerkin) solution is taken as the reference for comparison. In addition, the proposed approach is essentially a DG approach because the failure criterion is never reached and $\alpha = 0$ always.

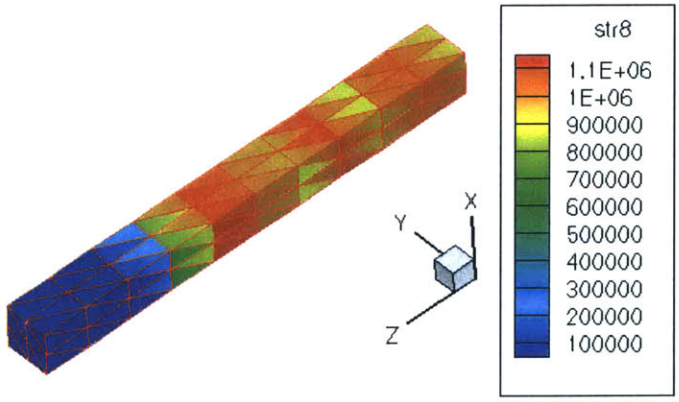

Figure 4-7: Propagation of a uniaxial tensile stress wave in the simple beam with interface elements in between all the bulk elements; contours correspond to σ_{33} stresses

To compare the three approaches, the time evolution of face 'a' velocity is plotted as shown in Figure 4-8. It shows that the in the case of cohesive interface approach the stress wave reaches the opposite end of the beam at a much later time. This shows that the cohesive formulation interferes with stress wave propagation in the pre-failure stage.

To avoid this problem, Espinosa and Zavattieri [48] have pointed that one could increase the stiffness of the interface element, represented by initial slope of the cohesive law, such that the wave speed in the material is not affected by the interface elements. As the slope of the function that specifies the traction-separation law increases, the wave speed in a material with DG method based cohesive interface elements reaches that of a material without any cohesive elements, as is desired in case of stress wave propagation in the absence of fracture. The cohesive interface

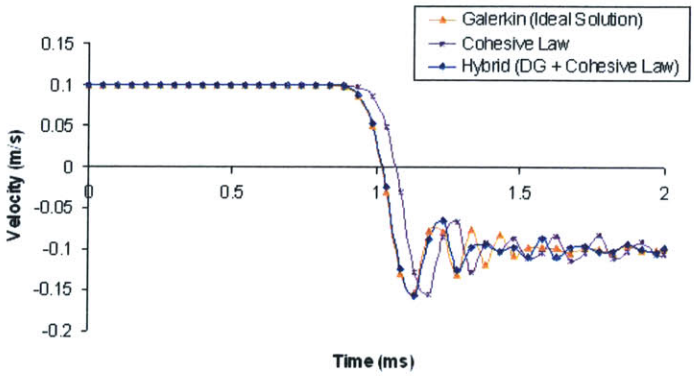

Figure 4-8: Time evolution of face 'a' velocity; figure shows that the tensile stress wave is delayed in the case of pure cohesive interface approach

approach and the proposed approach indeed yield similar results, as shown in Figure 4-9, when an appropriate stiffness for the cohesive law is used (σ_c = 6000 MPa and $\delta_c = 5.46\text{x}10^{-6}$m).

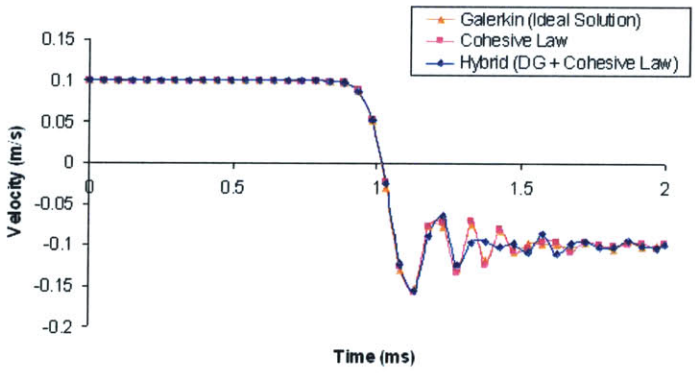

Figure 4-9: Time evolution of face 'a' velocity; figure shows that for an appropriate choice of the cohesive law, both the cohesive and proposed approaches yield similar results

However, as pointed out in Espinosa and Zavattieri [48], the increase of stiffness comes accompanied with a decrease of the stable time step of the dynamic simulation.

Table 4.3: Comparison of the stable time step values for different interface approaches in the stress wave propagation problem

Formulation	Stable time step, Δt_s
Continuous Galerkin	5.9014 μs
Interface layer only at the middle of the beam:	
Purely cohesive	1.1803 μs
DG method based cohesive	5.9014 μs
Interface layer between all bulk elements:	
Purely cohesive	0.5311 μs
DG method based cohesive	3.3638 μs

For the problem considered here, Table 4.3 gives the comparison between the stable time steps. For this comparison, the parameter values of Table 4.2 were used. The stable time step for the pure cohesive law approach in this case is about 6 times smaller than that required for the hybrid law. For more complex problems, this difference in stable time steps presents a substantial advantage in simulation time for the DG method based approach.

Thus the initial slope of the cohesive law has to be large enough to mask the disparity between the interface layer and bulk elements in wave propagation, but small enough so as to be numerically stable for a given stable time-step. It should also be noted that the assumption that the traction-separation law is characteristic for the material is being violated. A different approach proposed is to dynamically check for the traction on the interface of two bulk elements and introduce a cohesive element between them only when the failure criterion is satisfied. However, this is a very complex proposition, especially since the incremental addition of interface elements is difficult to parallelize. Instead, by using the proposed DG framework

based approach, the effects on stress-wave propagation in the pre-failure stage are completely discarded. The dependence of the stable time-step on the initial slope of the cohesive law is also eliminated. Since the proposed formulation is implemented in the DG framework itself, the computational advantages of DG methods including scalability as mentioned in Section 4.1 are inherited.

Chapter 5

Conclusion

5.1 Summary and conclusions

The Mannesmann effect has been simulated using the GTN model. The tensile stress state at the center of the cylinder has been verified. The plastic strain profiles, evolution of porosity, contribution of nucleation of new voids and growth of existing voids to the total VVF and its evolution have been analyzed. A parametric study has been done to see how the parameters influence the results of the Mannesmann process simulation. For a set of parameter values, it has been demonstrated that fracture will occur at the center of the cylinder. The shape of the deformed body, the analysis of the stress profiles, strain profiles and the porosity distribution verify the correctness of the simulations and the applicability of the model to the Mannesmann process. However, the model overestimates the amount of diameter reduction required for void formation at the center. This is because the values of the parameters used are not calibrated to the Mannesmann conditions. The ranges of values reported in literature

of these parameters do not correspond to high temperature, low stress triaxiality conditions. With the help of a set of experiments and numerical simulations, the calibration can be done. Weighted accumulated plastic strain fracture criteria have been implemented, and the critical damage constants have been calculated.

The formulations for the discontinuous Galerkin method, cohesive interface approach and a combined method based on these two approaches have been presented. The DG based cohesive interface formulation avoids the introduction of non-physical terms in the pre-failure regime. It also presents some advantages in terms of the stable time step and scalability of the computational modeling. It has been implemented for a simple specimen under uniaxial loading conditions. The advantages of the proposed method over that of pure cohesive interface approach have been demonstrated.

It must be noted that in general the interface models do not explicitly account for the effects of effective plastic strain or the stress triaxiality on ductile fracture.Because the cohesive law is a phenomenological representation of the ductile fracture processes of void growth and coalescence, and the creep behavior at high temperature, all these effects can in principle be accounted for in the interface approach by modifying the cohesive law to be dependent on parameters such as stress triaxiality and effective plastic strain of the adjacent bulk elements.

5.2 Future work

The GTN model parameters and the damage limits of the weighted accumulated plastic strain criteria need to be calibrated for the Mannesmann process. The *hybrid*

interface model that has been demonstrated for a simple beam under tensile loading can be applied for the more complex geometry of Mannesmann process. The creep behavior of the material can be taken into account explicitly. At the expense of complicating the model, polycrystal plasticity can be considered and competition between intra and inter-grain boundary ductile fracture can be studied.

Bibliography

[1] D.A. Berazategui, M.A. Cavaliere, L. Montelatici, and E.N. Dvorkin. On the modeling of complex 3D bulk metal forming processes via the pseudo-concentrations technique. Application to the simulation of the Mannesmann piercing process. *International Journal for Numerical Methods in Engineering*, 65:1113–1144, 2006.

[2] E. Erman. The influence of the processing parameters on the performance of the two-roll piercing operation. *Journal of Mechanical Working Technology*, 15:167–179, 1987.

[3] Q. Li, M.R. Lovell, W. Slaughter, and K. Tagavi. Investigation of the morphology of internal defects in cross wedge rolling. *Journal of Materials Processing Technology*, 125-126:248–257, 2002.

[4] G. Pantiu and T. Perez. Analysis of central fracturing in piercing. Comparison of samples pierced at the Mar del Plata tribological simulator and during SIDERCA plant trials. Technical report, CINI, 2005.

[5] S. Urbanski and J. Kazanecki. Assessment of the strain distribution in the rotary piercing process by the finite element method. *Journal of Materials Processing Technology*, 45:335–340, 1994.

[6] G. Capoferri, E. Ceretti, C. Giardini, A. Attanasio, and F. Brisotto. FEM analysis of rotary tube piercing process. *Tube and Pipe Technology*, pages 55–58, 2002.

[7] E. Ceretti, C. Giardini, and F. Brisotto. 2D simulation and validation of rotary tube piercing process. In *Proceedings of the 8th International Conference on Numerical Methods in Industrial Forming Processes*, volume 712, pages 1154–1159, 2004.

[8] E. Ceretti, C. Giardini, A. Attanasio, F. Brisotto, and G. Capoferri. Rotary tube piercing study by FEM analysis: 3D simulations and experimental results. *Tube and Pipe Technology*, pages 55–58, 2004.

[9] J. Pietsch and P. Thieven. FEM simulation of the rotary tube piercing process. *MPT International*, pages 52–60, 2003.

[10] K. Komori. Simulation of Mannesmann piercing process by the three-dimensional rigid-plastic finite-element method. *International Journal of Mechanical Sciences*, 47:1838–1853, 2005.

[11] Z. Pater, J. Kazanecki, and J. Bartnicki. Three dimensional thermo-mechanical simulation of the tube forming process in Diescher's mill. *Journal of Materials Processing Technology*, 177(1–3):167–170, 2006.

[12] F.A. McClintock. A criterion for ductile fracture by the growth of holes. *Journal of Applied Mechanics*, 27:363–371, 1968.

[13] J.R. Rice and D.M. Tracey. On the ductile enlargement of voids in triaxial stress fields. *Journal of the Mechanics and Physics of Solids*, 17(2):201–217, 1969.

[14] J.R. Rice and G.F. Rosengren. Plane strain deformation near a crack tip in a power-law hardening material. *Journal of the Mechanics and Physics of Solids*, 16(1):1–12, 1968.

[15] J.W. Hutchinson. Singular behavior at the end of a tensile crack in a hardening material. *Journal of the Mechanics and Physics of Solids*, 16(1):13–31, 1968.

[16] C.E. Turner and O. Kolednik. Application of energy dissipation rate arguments to stable crack growth. *Fatigue and Fracture of Engineering Materials and Structures*, 17:1109–1127, 1994.

[17] N.P. O'Dowd and C.F. Shih. Family of crack-tip fields characterized by a triaxiality parameter I: Structure of fields. *Journal of the Mechanics and Physics of Solids*, 39(8):989–1015, 1991.

[18] N.P. O'Dowd and C.F. Shih. Family of crack-tip fields characterized by a triaxiality parameter II: Fracture applications. *Journal of the Mechanics and Physics of Solids*, 40(8):939–963, 1992.

[19] S. Hao, A. Cornec, and K.H. Schwalbe. Plastic stress-strain fields and limit loads of a plane strain cracked tensile panel with a mismatched welded joint. *International Journal of Solids and Structures*, 34(3):297–326, 1997.

[20] Y. Shi, S. Sun, H. Murakawa, and Y. Ueda. Finite element analysis on relationships between the J-integral and CTOD for stationary cracks in welded tensile specimens. *International Journal of Pressure Vessels and Piping*, 75:197–202, 1998.

[21] K.E. Puttick. Ductile fracture in metals. *Philosophical Magazine*, 4:964–969, 1959.

[22] A.L. Gurson. Continuum theory of ductile rupture by void nucleation and growth: Part I- Yield criteria and flow rules for porous ductile media. *Journal of Engineering Materials and Technology*, 99:2–15, 1977.

[23] C.C. Chu and A. Needleman. Void nucleation effects in biaxially stretched sheets. *Journal of Engineering Materials and Technology*, 102:249–256, 1980.

[24] V. Tvergaard. Ductile fracture by cavity nucleation between larger voids. *Journal of the Mechanics and Physics of Solids*, 30(4):265–286, 1982.

[25] V. Tvergaard. On localization in ductile materials containing spherical voids. *International Journal of Fracture*, 18(4):237–252, 1982.

[26] V. Tvergaard and A. Needleman. Analysis of the cup-cone fracture in a round tensile bar. *Acta Metallurgica*, 32(1):157–169, 1984.

[27] A. Needleman and V. Tvergaard. An analysis of ductile rupture in notched bars. *Journal of the Mechanics and Physics of Solids*, 32(6):461–490, 1984.

[28] T.L. Anderson. *Fracture Mechanics: fundamentals and applications.* CRC Press, 1995.

[29] O. Richmond R. Becker, A. Needleman and V. Tvergaard. Void growth and failure in notched bars. *Journal of the Mechanics and Physics of Solids*, 36(3):317–351, 1988.

[30] Hibbitt, Karlsson & Sorensen Inc., Pawtucket, RI 02860. *ABAQUS/Explicit User's Manual, Version 6.5*, 2005.

[31] A. Corigliano, S. Mariani, and B. Orsatti. Identification of Gurson - Tvergaard material model parameters via Kalman filtering technique. I. Theory. *International Journal of Plasticity*, 104:349–373, 2000.

[32] A. Zavaliangos and L. Anand. Thermal aspects of shear localization in microporous viscoplastic solids. *International Journal for Numerical Methods in Engineering*, 33:595–634, 1992.

[33] A. Zavaliangos and L. Anand. Thermal aspects of shear localization in microporous viscoplastic solids. *Journal of the Mechanics and Physics of Solids*, 41:1087–1118, 1993.

[34] Y. Bao and T. Wierzbicki. A comparative study on various ductile crack formation criteria. *Journal of Engineering Materials and Technology*, 126:314–324, 2004.

[35] Y. Bao and T. Wierzbicki. On fracture locus in the equivalent strain and stress triaxiality space. *International Journal of Mechanical Sciences*, 46:81–98, 2004.

[36] J. Besson, D. Steglich, and W. Brocks. Modeling of crack growth in round bars and plane strain specimens. *International Journal of Solids and Structures*, 38:8259–8284, 2001.

[37] D.Z. Sun, D. Siegele, B. Voss, and W. Schmitt. Microcrack coalescence and macroscopic crack growth initiation in brittle solids. *Fatigue and Fracture of Engineering Materials and Structures*, 12(3):201–212, 1989.

[38] Z.L. Zhang. A sensitivity analysis of material parameters for the Gurson constitutive model. *Fatigue and Fracture of Engineering Materials and Structures*, 19(5):561–570, 1996.

[39] J. Faleskog, X. Gao, and C.F. Shih. Cell model for nonlinear fracture analysis - I. Micromechanics calibration. *International Journal of Fracture*, 89:355–373, 1998.

[40] J. Faleskog, X. Gao, and C.F. Shih. Cell model for nonlinear fracture analysis - II. Fracture-process calibration and verification. *International Journal of Fracture*, 89:375–398, 1998.

[41] J. Koplik and A. Needleman. Void growth and coalescence in porous plastic solids. *International Journal of Solids and Structures*, 24:835–853, 1988.

[42] W. Brocks, D.Z. Sun, and A. Hönig. Verification of the transferability of micromechanical parameters by cell model calculations with visco-plastic materials. *International Journal of Plasticity*, 11:971–989, 1995.

[43] T. Pardoen, T. Doghri, and F. Delannay. Experimental and numerical comparison of void growth models and void coalescence criteria for the prediction of ductile fracture in copper bars. *Acta Materialia*, 46:541–552, 1998.

[44] T. Pardoen and J.W. Hutchinson. An extended model for void growth and coalescence. *Journal of Mechanics and Physics of Solids*, 46:2467–2512, 2000.

[45] M. Gologanu, J.B. Leblond, G. Perrin, and J. Devaux. Recent extensions of Gurson's model for porous ductile metals. In P. Suquet, editor, *Continuum Micromechanics*. Springer-Verlag, 1995.

[46] M. Ortiz and A. Pandolfi. Finite-deformation irreversible cohesive elements for three-dimensional crack propagation analysis. *International Journal of Numerical Methods in Engineering*, 44:1267–1282, 1999.

[47] A. Pandolfi, P. Krysl, and M. Ortiz. Finite element simulation of ring expansion and fragmentation: The capturing of length and time scales through cohesive models of fracture. *International Journal of Fracture*, 95:279–297, 1999.

[48] H.D. Espinosa and P.D. Zavattieri. A grain level model for the study of failure initiation and evolution in polycrystalline brittle materials. Part I: Theory and numerical implementation. *Mechanics of Materials*, 35:333–364, 2003.

[49] L. Noels and R. Radovitzky. A general discontinuous Galerkin method for finite hyperelasticity. Formulation and numerical applications. *International Journal of Numerical Methods in Engineering*, 68(1):64–97, 2006.

[50] G. Engel, K. Garikipati, T.J.R. Hughes, M.G. Larson, L. Mazzei, and R.L. Taylor. Continuous/discontinuous finite element approximations of fourth-order elliptic problems in structural and continuum mechanics with applications to thin beams and plates. *Computer Methods in Applied Mechanics and Engineering*, 191:3669–3750, 2002.

[51] S. Guzey, H.K. Stolarski, B. Cockburn, and K.K. Tamma. Design and development of a discontinuous Galerkin method for shells. *Computer Methods in Applied Mechanics and Engineering*, 195:3528–3548, 2006.

[52] J. Mergheim, E. Kuhl, and P. Steinmann. A hybrid discontinuous Galerkin/interface method for the computational modeling of failure. *Communications in Numerical Methods in Engineering*, 20:511–519, 2004.

[53] L. Molari, G.N. Wells, K. Garikipati, and F. Ubertini. A discontinuous Galerkin method for strain gradient-dependent damage: Study of interpolations and convergence. *Computer Methods in Applied Mechanics and Engineering*, 195:1480–1498, 2006.

[54] L. Noels and R. Radovitzky. An explicit discontinuous Galerkin method for non-linear solid dynamics. Formulation, parallel implementation and scalability. *International Journal of Numerical Methods in Engineering*, 2006.

[55] J.E. Marsden and T.J.R. Hughes. *Mathematical foundations of elasticity.* Dover Publications, 1993.

[56] D.S. Dugdale. Yielding of steel sheets containing slits. *Journal of Mechanics and Physics of Solids*, 8:100–104, 1960.

[57] G.I. Barrenblatt. The mathematical theory of equilibrium of cracks in brittle fracture. *Advances in Applied Mechanics*, 7:55–129, 1962.

[58] G. T. Camacho and M. Ortiz. Computational modeling of impact damage in brittle materials. *International Journal of Solids and Structures*, 33(20):2899–2938, 1996.

[59] K. Willam. Simulation issues of distributed and localized failure computations. In *Cracking and Damage*, pages 363–378. Elsevier Science, 1989.

[60] X. P. Xu and A. Needleman. Numerical simulations of fast crack growth in brittle solids. *Journal of Mechanics and Physics of Solids*, 42(9):1397–1407, 1994.